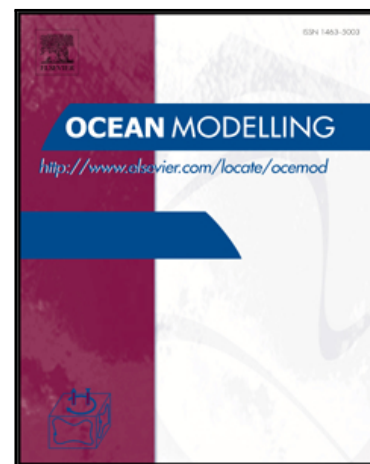# Accepted Manuscript

Submesoscale currents in the Northern Gulf of Mexico: Deep
phenomena and dispersion over the continental slope

Annalisa Bracco , Jun Choi , Keshav Joshi , Hao Luo ,
James C. McWilliams

Highlights

- The northern Gulf of Mexico circulation is simulated at two horizontal resolutions.
- Mechanisms for submesoscale currents along continental slopes are investigated.
- Submesoscale structures consist of frontal along-slope currents and eddies.
- Submesoscale dynamics impact representation of mixing.

Submesoscale currents in the Northern Gulf of Mexico: Deep phenomena and dispersion over the continental slope

Annalisa Bracco[1], Jun Choi[1], [*], Keshav Joshi[1,2], Hao Luo[1,3], James C. McWilliams[4]

[1] School of Earth and Atmospherics Sciences, Georgia Institute of Technology, Atlanta, GA 30332, USA

[2] School of Physics, Georgia Institute of Technology, Atlanta, GA 30332, USA

[3] Department of Marine Sciences, University of Georgia, Athens, GA 30602, USA

[4] Department of Atmospheric and Oceanic Sciences, University of California, Los Angeles, CA 90095, USA

Corresponding Author:

Annalisa Bracco, School of Earth and Atmospheric Sciences,

311 Ferst Dr, Atlanta, GA, 30332, USA

email: abracco@gatech.edu

Ph: 404-894-1749

Abstract

This study examines the mesoscale and submesoscale circulations along the continental slope in the northern Gulf of Mexico at depths greater than 1000 m. The investigation is performed using a regional model run at two horizontal grid resolutions, 5 km and 1.6 km, over a three year period, from January 2010 to December 2012.

Ageostrophic submesoscale eddies and vorticity filaments populate the continental slope, and they are stronger and more abundant in the simulation at higher resolution, as to be expected. They are formed from horizontal shear layers at the edges of highly intermittent, bottom-intensified, along-slope boundary currents and in the cores of those currents where they are confined to steep slopes. Two different flow regimes are identified. The first applies to the De Soto Canyon that is characterized by weak mean currents and, in the high-resolution run, by intense but few submesoscale eddies that form near preferentially along the Florida continental slope. The second is found in the remainder of the domain, where the mean currents are stronger and the circulation is highly variable in both space and time, and the vorticity field is populated, in the high-resolution case, by numerous vorticity filaments and short-lived eddies.

Lagrangian tracers are deployed at different times along the continental shelf below 1000 m depth to quantify the impact of the submesoscale currents on transport and mixing. The modeled absolute dispersion is, on average, independent of horizontal resolution, while mixing, quantified by finite-size Lyapunov exponents and vertical relative dispersion, increases when submesoscale processes are present. Dispersion in the De Soto Canyon is smaller than in the rest of the model domain and less affected by resolution. This is further confirmed comparing the evolution of passive dye fields deployed in De Soto Canyon near

the Macondo Prospect, where the *Deepwater Horizon* rig exploded in 2010, and at the largest known natural hydrocarbon seep in the northern Gulf, known as GC600, located a few hundred kilometers to the west of the rig wellhead.

1. Introduction

Processes and dynamics occurring in oceanic submesoscale currents (horizontal length scales between ~ 100 m and ~ 10 km, and time scales between a few hours and a few days) have been shown to impact stirring and dispersion of natural and anthropogenic tracers in the upper ocean. Submesoscale circulation patterns can modify the mixed-layer stratification, and manifest as ageostrophic fronts and, whenever these fronts are unstable, meanders and eddies (Capet et al., 2008b; Fox-Kemper et al., 2008; McWilliams et al., 2009a; Taylor and Ferrari, 2011; Thomas et al., 2008). The generation of submesoscale fronts and consequent instabilities has been investigated in a number of papers (Capet et al., 2008a; Haine and Marshall, 1998; Holmes et al., 2014; McWilliams et al., 2009b; Thomas and Ferrari, 2008; Thomas et al., 2013).

A heuristic description of front generation relevant to this work is presented in Lévy et al. (2012). Submesoscale ageostrophic frontogenesis arises whenever the steepness of density surfaces approaches O(1) (Capet et al., 2008b). In the oceanic interior any density anomaly generated by the stirring and straining of the mesoscale field is quickly damped by

overturning circulations that reduce the local steepness in the density field to restore geostrophic balance, with the end result that almost flat density surfaces are maintained (Klein et al., 2008). At the top and bottom of the ocean, on the other hand, those overturning circulations cannot effectively reduce the density fronts generated by the mesoscale turbulence due to the presence of the air-sea and bottom boundaries, and the fronts sharpen (Lévy et al., 2012). Such sharpening leads to submesoscale frontogenesis and eventually to ageostrophic secondary circulations that limit frontal intensification by generating submesoscale eddies (Fox-Kemper et al., 2008).

Several recent studies attempt to characterize submesoscale dynamics near the oceanic surface (Boccaletti et al., 2007; Capet et al., 2008a,b; Thomas and Ferrari, 2008; Thomas et al., 2008) and to quantify their role on the transport and mixing with numerical tools (Gula et al., 2014; Klein and Lapeyre, 2009; Koszalka et al., 2009; Lévy et al., 2010; Lévy et al., 2011; Zhong et al., 2012; Zhong and Bracco, 2013) and with targeted field campaigns (D'Asaro et al., 2011; Poje et al., 2014; Shcherbina et al., 2013).

Little is known, however, about those dynamics and their effects at depth, near the sea floor, with the exception of the California Current System, where numerical simulations have shown that ageostrophic submesoscale motions contribute to the generation of long-lived subsurface anticyclones through centrifugal instability (Dewar et al., 2015; Molemaker et al., 2015). In this work we investigate the impact of submesoscale dynamics along the continental slope in the northern Gulf of Mexico (hereafter GoM).

The GoM basin is characterized by a broad, highly variable slope that hosts a large number of natural hydrocabon seeps (Garcia-Pineda et al., 2009; Peccini and MacDonald, 2008;) found predominantly at depths greater than 1000 m. It was impacted by the largest deep-

water oil spill ever recorded following the explosion of the *Deepwater Horizon* rig on April 20, 2010. The spill discharged approximately 3 x 10^8 kg of gas and between 6 and 8 x 10^8 kg of oil, about a third of which was confined in underwater plumes found in several layers between 700 m and the oceanic seafloor (Joye et al., 2011).

In this paper we address two main questions with the goal of improving our understanding of transport and mixing along continental slopes:

- Are submesoscale dynamics relevant to the circulation along the continental slope in the northern Gulf of Mexico, and if so what are the mechanisms responsible for their generation?

- Which role, if any, does model resolution play in the representation of transport and mixing of passive, neutrally buoyant tracers released along the slope?

We consider two simulations of the northern Gulf of Mexico, performed with 5 km and 1.6 km horizontal grid resolutions and spanning three years, from January 2010 to December 2012; the first resolves fully the mesoscale dynamics, while the second one is submesoscale permitting (i.e., has partial resolution). We concentrate on dynamics relevant for the deep layer in the GoM, considering only depths equal or greater than 1000 m. After analyzing the vorticity structures that characterize the flow in the two runs, we present dispersion statistics from an ensemble of deployments of neutrally buoyant Lagrangian particles released along the continental slope. Finally, we discuss the evolution of Eulerian passive tracers deployed at two sites over one year, and quantify the tracer diffusivities. While the simulations we consider are not directly relevant to the 2010 oil spill --- particular realizations of oceanic eddies are inherently unpredictable without observational constraints

--- the answers to the questions above may guide better hindcasting and forecasting capabilities for deep pollutant releases.

2. Model setup, domain and forcing fields

The Gulf of Mexico circulation is simulated with the Regional Oceanic Modeling System (ROMS) in the version developed by the Institut de Recherche pour le Développement (IRD), ROMS-Agrif 2.2 (Debreu et al., 2012). The model domain covers the whole Gulf of Mexico (GoM), but we concentrate on its northern portion and specifically on the area comprised between 96.31^{o}W - 86.93^{o}W and 25.40^{o}N - 30.66^{o}N, indicated as northern GoM in the following (Fig. 1). This region contains a large number of natural hydrocarbon seeps (MacDonald et al., 2002) and coincides with the area that was the most affected by the *Deepwater Horizon* spill in 2010 (Joye et al., 2011). In this work we consider two integrations differing only in their horizontal grid resolutions of 5 km (LR, for Low Resolution) and 1.6 km (HR, for High Resolution). HR is obtained exploiting the two-way nesting capabilities of ROMS-Agrif 2.2 in the focus area. The vertical resolution is 70 stretched, terrain-following layers, and is enhanced near the surface and the bottom. The enhancement near the bottom together with the implementation of the pressure-gradient algorithm proposed by Shchepetkin and McWilliams (2003) based on a high order density profile reconstruction and on the rewriting of the equation of state to reduce spurious water compressibility effects, reduce pressure-gradient errors over steep topography (Beckman and Haidvogel, 1993). The depth of the bottom layer varies across the domain and in waters deeper than 1000 m varies between 35 and 75 m. The model bathymetry is derived from the 2 min Gridded Global Relief Data Collection topography ETOPO2 (Sandwell and Smith,

1997), interpolated at 5 km and modified applying iteratively a logarithmic Shapiro to

obtain a maximum slope parameter $r \sim \dfrac{\nabla h}{h} = 0.35$ (Penven et al., 2008). The chosen r is

greater than the recommended 0.25 (Penven et al., 2008), however tests performed with the

5 km model set-up used in Cardona and Bracco (2014) showed that in the Gulf of Mexico

domain it represents a good compromise between limiting pressure gradient errors and

obtaining near bottom currents that compare well with observations in both speed and

variability (see Appendix). In the nested solution the bathymetry is interpolated from its 5

km version, so that no new, small-scale topographic features are added, with an effectively

smaller slope parameter (in the steepest portions of the domain r is less or equal to 0.23 in

the HR case). Both runs span three years, from January 2010 to December 2012, and they

are identically forced by 6-hourly momentum and 12-hourly heat fluxes from the ERA-

Interim reanalysis (Dee et al., 2011). The open-ocean boundaries are nudged to the monthly

fields from the HYCOM – NCODA (Hybrid Coordinate Ocean Model - Navy Coupled

Ocean Data Assimilation) oceanic prediction system (GOMl0.04 expt. 30.1, http:

//www7320.nrlssc.navy.mil/hycomGOM). Fresh water fluxes are prescribed by nudging

surface salinity to the World Ocean Atlas 2009 (WOA09) monthly varying climatology

(Antonov et al., 2010) without any synoptic or interannual variability. A non-local, K-

profile planetary (KPP) boundary layer scheme (Large et al., 1994) is implemented to

parameterize the unresolved vertical subgrid-scale processes. Turbulence at the bottom is

damped by quadratic bottom drag with coefficient $C_d = 0.003$. Further information about the

model configuration, spin-up, and validation can be found in Luo et al. (2015) (LBCM in

the following). Configuration and forcing files are also available through the Gulf of

Mexico Research Initiative Information and Data Cooperative (GRIIDC), doi: 10.7266/N7028PF7.

In both integrations transport and mixing properties are investigated using Lagrangian and Eulerian tracers. Our focus is De Soto Canyon, the region where the *Deepwater Horizon* oil drilling rig was located, and Green Canyon, an area to the west of the Mississippi Fan that extends into the Central Slope and is rich in oil fields. We released 8,855 neutrally buoyant Lagrangian particles (one per grid point in the HR grid) in the HR and LR simulations on April 20, 2010 and then every 10 days thereafter for a total of six deployments (Fig. 2). The particles are released in the model bottom layer along the continental slope uniformly from -91.3 to -87.5^{o}W at depths comprised between 1200 and 2000 m. Trajectories are then integrated for 100 days. At depths greater than 1000 m the cumulative Eulerian time scale,

$$T_E = \int_0^\infty r_e(\tau)d\tau \text{ where } r(\tau) = \lim_{\Gamma \to \infty} \left[\frac{\frac{1}{\Gamma}\int_0^\Gamma u'(t)u'(t+\tau)dt}{\frac{1}{\Gamma}\int_0^\Gamma u'^2(t)dt} \right], \text{ is about 20 days in the De Soto}$$

Canyon and 15 days along the remaining northern slope, in agreement with previous estimates by Cardona and Bracco (2014). Each Lagrangian deployment spans therefore at least five T_e. The tracers are released in the model bottom layer and are tracked off-line using LTRANS v.2b (Schlag and North, 2012) using hourly-averaged three dimensional velocity fields. We verified that the error introduced by using off-line tracking (Keating et al., 2011) is negligible when using hourly fields by comparing on-line and off-line trajectories in ten days long integrations. Subsequent analysis of the trajectories quantify transport and mixing properties for particles grouped according to their release location (regions A and B in Fig. 2).

We also simulate the release of an Eulerian tracer at Mississippi Canyon Block 297 (abbreviated MC297) (-88.36$^{\text{o}}$W, 28.70$^{\text{o}}$N, depth 1562 m), a site 6 km to the south-southeast of MC252, the location of the *Deepwater Horizon* rig. A second release is carried out at Green Canyon Block 600 (GC600, -90.57$^{\text{o}}$W, 27.36$^{\text{o}}$N, depth 1249.3 m), the largest natural oil and gas seep in the northern Gulf located at roughly the same water depth of MC252 but to the west of the Mississippi Fan, along the eastern edge of the Central Slope. Both deployment sites have been visited regularly by cruises of the ECOGIG consortium (https://ecogig.org) between 2010 and 2013. The Eulerian tracers are released on April 20, 2010 and are advected for 12 months. The tracer advection is performed using a split tracer advection and diffusion scheme and rotated biharmonic diffusion with flow-dependent hyperdiffusivity that satisfies the Peclet constraint (Lemarié et al., 2012; Marchesiello et al., 2009) to minimize spurious diapycnal mixing while preserving water mass characteristics.

3. Mean Circulation at depth

The circulation in the Gulf can be approximated by a two-layer system. The top layer extends approximately over the upper 1000 m and its circulation is dominated by the anticyclonic Loop Current and the Rings or Loop Eddies that detach from it every ten-eleven months on average (Vukovich, 2007), together with associated pycnocline mesoscale and surface-layer submesoscale currents. Underneath, the mean flow is cyclonic around the basin away from the continental slope, as indicated by current-meter observations, Lagrangian circulation (PALACE) floats, and the basin temperature structure (DeHaan and Sturges, 2005; Hamilton, 1990; Weatherly, 2004). In-situ measurements reveal that vortex stretching and topographic Rossby waves (TRWs) with periodicities ranging from 10 to 50

days contribute to the instantaneous deep flow of the northern Gulf (DeHaan and Sturges, 2005; Hamilton, 2009; Kolodziejczyk et al., 2012; Pérez-Brunius et al., 2013). TRWs in particular are responsible for the bottom intensification of currents aligned and trapped along the continental slope where the bathymetry is steep (Dukhovskoy et al., 2009; Hamilton, 2007; Hamilton and Lugo-Fernandez, 2001).

Model simulations confirm the mean flow direction (Cardona and Bracco, 2014; Lee and Mellor, 2003) and the approximate periodicity of the intra-seasonal variability (see also Appendix). Fig. 3 shows the modeled mean velocities at 1500 m depth superimposed on the mean speed, $\sqrt{\bar{u}^2 + \bar{v}^2}$, where $\bar{u}(x, y)$ and $\bar{v}(x, y)$ are the horizontal velocity components time-averaged over the integration period. A cyclonic current dominates the circulation south of 26°N. Over the slope the mean flow consists of numerous closed recirculations generated by the interaction with the complex bathymetry, with similar patterns in the two integrations. The mean speed at 1500 m in Fig. 3, while representing only a small portion of the total kinetic energy of the flow, is about 35% higher in HR than in LR. The difference in mean speeds should not be attributed to resolution, but is more an expression of the intrinsic variability of the system, likely linked to the different realizations of the upper layer dynamics in relation to the modeled LC variability[1]. The cyclonic current pattern south of 26.3°N over the deeper portion of the basin is the most prominent feature in the mean flow independent of resolution, and it is a major contributor to the HR versus LR mean speed amplitude difference. This current is coherent throughout the deep layer in agreement with the analysis of trajectories from 36 RAFOS floats deployed from April 2003 to April 2004

---

[1] We have verified that the mean speed of a different 8-year long run at 5 km resolution presented in Cardona and Bracco (2014) is indeed comparable to HR in both patterns and intensity.

at depths between 1000 and 3000 m (Hamilton, 2009). Additionally, its amplitude increases with depth, both in the model and in the observations.

Despite the identical atmospheric forcing and boundary conditions, the mesoscale dynamics and in particular the Loop Current evolution are not deterministic (Cardona and Bracco, 2014), and the outcomes differ in the two runs (LBCM); note that no observational data are assimilated. The domain averaged eddy kinetic energy (EKE) differs between HR and LR, and it is slightly larger in HR. The greater amplitude of the instantaneous velocity field in HR in most locations compares better with the (limited) available observations (DeHaan and Sturges, 2005; Hamilton and Lugo-Fernández, 2001; Oey and Hamilton, 2012; Weatherly, 2004). Modeled near-bottom velocities are further validated in the Appendix.

EKE time series at various depths are shown in Figure 4. They are calculated as $\frac{1}{2}\left(\left\langle u'^2 + v'^2 \right\rangle\right)$, where $\langle\rangle$ designates spatial averaging over the northern Gulf (96.31$^{\mathrm{o}}$W - 86.93$^{\mathrm{o}}$W and 25.40$^{\mathrm{o}}$N - 30.66$^{\mathrm{o}}$N) and $u'(x,y)$ and $v'(x,y)$ are obtained subtracting the time mean velocity components at each grid point, $\bar{u}(x, y)$ and $\bar{v}(x, y)$. The time series highlight the increase of EKE with depth, its coherency through the deep layer, and its intensification at irregular intervals between 2-7 months in both runs. The EKE peaks have comparable amplitudes in HR and LR, and they are associated with the intermittent strengthening of the along-slope current system contributing to the recirculation region centered at -89.5$^{\mathrm{o}}$W, and with the formation of a mesoscale cyclone as discussed in the next section. Large velocity fluctuations with a time-scale comparable to the modeled ones have been recorded in the same area (Hamilton and Lugo-Fernández, 2001), but their generation mechanism remains unexplained. As noted in Cardona and Bracco (2014), the deep Gulf

circulation does not exhibit any seasonality, and the EKE variability below 1000 m is uncorrelated to the surface EKE (see Figure A.1 in LBCM for the surface EKE time series in both HR and LR runs).

4. Mesoscale and submesoscale dynamics at depth

4.1 Formation of mesoscale cyclones at Mississippi Fan

Two typical snapshots of relative vorticity normalized by the Coriolis parameter, ζ/f, depth-averaged between 1000 and the oceanic bottom, are shown in Fig. 5 (September 2011 in HR and August 2010 in LR). Both snapshots include the occurrence of the largest, strongest ($\zeta \geq 0.8\,f$) feature found in the deep layer in the northern Gulf: a bottom intensified mesoscale cyclone that forms at the Mississippi Fan. The episodic generation of this cyclonic eddy is indicated by the black dots in the EKE time series.

The cyclone formed at the Fan is coherent throughout the lower layer and bottom-intensified, as indicated by the synchronous peaks in the EKE time-series in Fig. 4. The vorticity generation at the Fan results from the interaction of the temporally varying current and the bathymetry. Analogous cyclogenesis has been detected using bottom current meters in the Kuroshio Extension (Greene et al., 2009). The along slope lower-layer flow to the west of the Fan is advected eastward contributing to the recirculation zone centered around -89.5^{o}W in Fig. 3. If the zonal velocity is weak, the flow is inhibited from moving over the seamount, but if the along-slope current is strong enough, the flow is advected over the topographic feature, where vortex lines are compressed and anticyclonic vorticity is generated as a

consequence of potential vorticity conservation, as in the case of the uniform flow impinging on a seamount modeled in Huppert and Bryan (1976) (Fig. 6 top panel). At the same time, for sufficiently strong currents, the fluid atop the Fan is advected eastward and cyclonic vorticity results from vortex stretching. The anticyclonic vorticity is trapped on the Fan (Fig. 6, middle panel), while the cyclone can drift downstream and away from the topographic feature until is entrained in the mean cyclonic current south of 26.3$^{\mathrm{o}}$N that brings it west (Fig. 6, middle and bottom panels; see also video of the 2500 m vorticity field in the Supplementary Material). The cyclone lifespan is between two and four weeks. The eddy first looses its strength moving south into deeper waters and then is dissipated by interactions with the bathymetry (see the vorticity videos at 1500 and 2500 m available as Supplementary Material).

Assuming that the lower layer is uniform and its potential vorticity (PV) is conserved, and that the relative vorticity atop the Fan is close to zero at times preceding the cyclone generation when local currents are weak, the strength of the cyclones can be evaluated considering the topographic stretching induced by the Fan, following Greene et al. (2009). The Fan extends between about 2700 and 1800 m, while the cyclonic PV anomaly extends upward to approximately 1000 m. The vorticity generated by stretching is therefore approximately

$$\varsigma = \left(\frac{H_{PVanom}}{H_{atop}} - 1 \right) f = \left(\frac{2700 - 1000}{1800 - 1000} - 1 \right) f \approx 1.1 f$$

The modeled relative vorticity at the cyclone cores in HR is indeed $1 \leq \frac{|\varsigma|}{f} \leq 1.3$ around 2700 m, depending on the event considered, and decreases to about 0.8 ± 0.1 at 1500 m. At the time of formation, the cyclone intensity depends on resolution and in LR the modeled Fan

eddies are weaker than in HR with maximum vorticity $|\zeta|/f \approx 0.9$. The vertical extent of the deep eddies is consistent with a scale $H \sim fL/N$, where L is the topographic feature width and N is the sub-pycnocline buoyancy frequency.

Owing to the resolution-dependent characteristics of these flow structures, the domain averaged ζ/f calculated using 360 instantaneous snapshots equally distributed over the three simulated years is more positive in HR than LR below 1000 m, as shown in left panel of Fig. 7. In the upper 1000 m, the anticyclonic vorticity of the Loop Current and Eddies dominate the domain averaged vorticity budget. In HR, however, the LC contribution is partially compensated in the mixed layer by submesoscale cyclonic eddies (see Fig. 7 in LBCM).

4.2 Submesoscale variability

In the submesoscale permitting run many cyclonic and anticyclonic eddies with radii comprised between 5 and 15 km occupy the continental slope (Fig. 5); those structures are weaker and far less numerous in LR. The PDFs of ζ/f calculated at various depths from 1000 to 2500 m indicate that both cyclonic and anticyclonic eddies and filaments contribute to the tail of the distributions, with a dominance of strong cyclonic structures and an increase in skewness in the HR simulation (Fig. 7; PDF shown for 1500 m). Model resolution plays an important role in the representation of those features with vorticity minima twice as large and maxima almost three times larger in HR than in LR; comparable resolution dependence characterizes the representation of vorticity extremes in the California Undercurrent domain (Molemaker et al., 2015). The kurtosis of the distributions is nearly twice as large in HR at all depths (18.4 and 9.7 at 1000 m, 15.7 and 8.9 at 1500 m, 12.4 and 6.8 at 2000 m, 11.9 and

6.3 at 2500 m in HR and LR, respectively). The enhancement of vorticity extremes and the doubling of kurtoses are of the same order of magnitude of those found at the surface (LBCM), but vorticity maxima and minima are two-three times smaller near the bottom than in the mixed layer in the northern Gulf of Mexico. In our configuration bottom friction limits the development of structures with $|\zeta/f| \gg 1$ at depth, while the inflow of freshwater fluxes through the Mississippi River system and the atmospheric forcing fuels frontogenesis at the surface.

Eddies and filaments populating the depth averaged vorticity field (Fig. 5) are generated along the GoM continental slope through instabilities of horizontal shear layers near the bottom, and therefore are best visualized in terrain-following coordinates. An example of near-bottom vorticity for depths greater than 1000 m at the two resolutions is given in Fig. 8. The corresponding lateral density gradients at the fixed depth of 1500 m are also shown. Enhanced density gradients are found in correspondence of the submesoscale structures in HR along the continental slope. Again, the relative increases in vorticity and lateral density gradients with resolution compare well with surface simulated fields, despite smaller absolute values.

Horizontal shear layers are responsible for the formation of the submesoscale eddies and filaments in HR. They often result from the juxtaposition of the strong and highly variable, zonal, front-like currents, characterized by large meridional density gradients where they impinge on the slope. An example is provided by the anticyclonic filament and cyclonic eddy at about 26.2°N and -93°W in Fig. 8. The zonal velocity in a meridional transect across this feature varies, from 26° to 26.5°N, from negative to positive and then to negative again

within 50 km (Fig. 9), while being moderate and negative in the three-year mean. For increasing *y,* negative vorticity is formed in presence of the wider positive $\frac{\partial u}{\partial y}$ gradient at the shear layer in correspondence of the first change in velocity sign. A partially unbalanced, stronger cyclone ($R_o = 0.85$ in its core) is then formed northward of it in correspondence of the negative gradient $\frac{\partial u}{\partial y}$ where a sharp density front is also found.

The intermittency found in the simulated zonal currents is representative of the variability observed in this region through mooring data (Hamilton, 2007; Kolodziejczyk et al., 2012). In the model runs the mean near-bottom velocity at or below 1000 m is westward over most of the northern Gulf (including over the Fan, while the anticyclonic recirculation appears at approximately 50 m above the bottom) and is similar in pattern and direction in HR and LR. The speed of near bottom currents in HR, however, is slightly greater than in the 5 km case everywhere but in the De Soto Canyon. In both runs the standard deviation (STD) is larger than the mean value, and bottom currents often reverse their direction (Fig. 10). The STD also increases from LR to HR, again with the exception of the De Soto region, with the consequent generation of more numerous and stronger eddies and filaments for increasing resolution in the central and western portion of the modeled domain.

In the HR simulation shear layers can be generated also according to the mechanism proposed in Molemaker et al. (2015) for the California Undercurrent. In this case they result from the drag exerted by bottom boundary layer parameterization, KPP, on the lowest model layer, where the velocity has to approach zero. Such drag is proportional to the square of the near bottom velocity itself (see schematic in Figure 7 in Molemaker et al., 2015). If the

current is sufficiently strong at the slope, then the resulting shear layer may support the generation of vertical vorticity of substantial amplitude. In the case of the GoM $\varsigma \approx -\dfrac{\partial u}{\partial y}$ at the slope, being the near bottom currents predominantly zonal, and the sign of the along-slope current corresponds to that of the bottom boundary layer. Whenever high values of vorticity are achieved ($|\zeta|/f > 0.4$), small scales eddies are generated. This mechanism is exemplified in Fig. 11 where a meridional transect on January 10, 2012 at approximately -90°W is shown. The vorticity filament is associated with the boundary layer where the zonal velocity of the jet-like current at 27.3^{o}N rapidly approaches zero at the sloping bottom. The boundary layer width is proportional to the boundary layer vertical thickness and inversely proportional to the cross-shelf bottom slope (Molemaker et al., 2015), and the horizontal boundary layer is partially resolved in HR and not resolved in LR.

5. Transport and mixing of passive tracers

The impact of horizontal resolution on the representation of tracer dispersion along the continental slope is quantified using Lagrangian tracers. In the subsequent analysis, the particles released near the bottom are grouped in two regions, according to their initial location. Region A covers De Soto Canyon, where the near-bottom speed and its variability are small; region B includes the Mississippi Fan and Mississippi Slope and the eastern portion of the Central Slope, where both mesoscale and submesoscale circulations are more intense.

Figure 12 shows the horizontal and vertical distribution of 3-D particles released on April 20 and June 10, 2010 in the two simulations 100 days past deployment. Movies of the lateral

evolution of the particles are available in the Supplementary Material. Most tracers released in region A remain in the De Soto Canyon unless they are seeded at the eastern edge of the Fan, where mesoscale advection provides an escape route (see videos). Particles initially in the Mississippi slope area (region B) spread over most of the domain. The majority of B tracers moves west over the Central Slope, while a small percentage penetrates the De Soto Canyon along the 1200 m isobath. In all deployments 1% or less of particles released in region B leaves the domain channeled through a narrow meridional strip at about -95.5^{o}W. The westward spreading for B particles varies within the six integrations due to the intermittency of the near bottom velocity field. This is exemplified by the two cases shown in Fig. 12.

To evaluate the flow transport properties, we computed the tracer absolute dispersion, A^2(t), along the three directions separately and in the horizontal. A^2(t) describes the time evolution of the square distance traveled by each particle, averaged over all particles and, in our case, over the 6 deployments. For example in the horizontal direction is defined as A^2(t) = <[$\mathbf{x}_i$(t)-$\mathbf{x}_i$(t$_0$)]^2>, where $\mathbf{x}_i$(t)=(x$_i$(t), y$_i$(t)) is the i-th particle (horizontal) position at time t, and t$_0$ is the deployment time. In homogeneous and stationary turbulent flows A^2(t) follows a ballistic regime ($A^2(t) \propto t^2$) (Taylor, 1921) for times shorter than the Lagrangian autocorrelation time T$_L$ (about 5 days in our domain), and a diffusive or Brownian regime ($A^2(t) \propto t$) at times much longer than T$_L$. Theoretical studies have tried to account for the presence of coherent eddies (Babiano et al., 1987; Provenzale, 1999) and found anomalous dispersion at intermediate times with $A^2(t) \propto t^{5/4}$ (Elhmaïdi et al., 1993) due to the presence of energetic circulation cells surrounding the eddies. The existence of this anomalous regime has been confirmed for eddy-dominated baroclinic (Berloff et al., 2002; Bracco et al., 2004),

and Boussinesq flows (Drake et al., 2011; Koszalka et al., 2009; Ohlmann and Mitarai, 2010; Zhong et al., 2013). In the ocean such scaling characterizes dispersion of floats in the Kuroshio Extension (Osborne et al., 1989) and in the Northeast Atlantic (Sanderson and Booth, 1991).

Figure 13 confirms that the representation of $A^2(t)$ is nonlocally controlled, as postulated by Taylor (1921), and determined by the mesoscale circulations, which are identically captured at both resolutions. In the horizontal plane the initial dispersion is ballistic during the first 3-5 day, followed by an anomalous intermediate regime and finally by the linear one, and is significantly smaller – as much as an order of magnitude in the zonal direction - for particles released in the De Soto Canyon. The zonal dispersion is larger than the meridional in region B and of the same order in region A. Overall, particles seeded outside De Soto are characterized by slightly larger zonal dispersions in HR than in LR over the last 50 days but differences are within the standard deviation of the six deployments. Region B is characterized by the greatest variability in zonal dispersion at times between one and two weeks, due to the large standard deviation in velocity field at the Mississippi Slope. Region A, on the other hand, displays largest meridional dispersion variability, as particles near the Fan can at times be transported south and into deeper waters by the mesoscale cyclones, and tracers deployed near the Florida slope may be transported along it.

Vertical dispersion of oceanic tracers cannot be investigated with floats, and numerical models provide the only tool for a systematic analysis, bearing in mind that they are limited in resolution and that the choice of vertical coordinate and advection and mixing schemes impacts the representation of vertical transport (Hill et al., 2012; Marchesiello et al., 2009). In our runs the horizontal model resolution does not impact significantly the representation

of vertical transport. High-resolution results are characterized by slightly larger vertical dispersions than the LR counterparts over the first ten days for particles in region B, but again differences are within the standard deviation of the six samples. All vertical dispersion curves follow a ballistic regime for short times. In De Soto different transients are detected, likely due to the inhomogeneity of the vertical velocity field throughout the steep continental slope of the canyon, and the vertical dispersion, likewise the lateral, is significantly lower than that of particles released outside the Canyon. In region B vertical dispersion transitions to a subdiffusive regime with $A_z^2(t) \propto 0.6$ for times longer than the Lagrangian autocorrelation. Results for region B agree with the theoretical and numerical work by van Aartrijk and co-authors (Aartrijk et al., 2008; van Aartrijk and Clercx, 2010) on vertical transport in idealized 3-D forced, stratified but nonrotating, and therefore without eddies, turbulent flows. They have shown that stratification arrests single particle dispersion in the direction of stratification, so that the Brownian regime is never attained and subdiffusive regimes are found instead.

To quantify lateral tracer spreading, we calculated the finite-size Lyapunov exponent (FSLE) (Artale et al., 1997). FSLE provides a measure of local stirring alternative to relative two-particle dispersion for nonhomogeneous flows in closed basins by computing the average time that particle pairs take to separate from a given scale δ to a scale αδ where α > 1 is a parameter, chosen to be 1.2 following previous works (Poje et al., 2010). FSLE has been used to separate mesoscale from submesoscale stirring in the ocean (d'Ovidio et al., 2009; Haza et al., 2012; Poje et al., 2014). A Richardson regime in relative dispersion (Richardson, 1926) translates in a FSLE slope $\lambda \sim \delta^{-2/3}$, while an exponential particle

separation, theoretically expected for the enstrophy cascade regime, translates in a flat plateau. A slope $\lambda \sim \delta^{-2}$ for separation scales much larger than the characteristic length scale of the velocity field indicates diffusive behavior. Any slope shallower than -2, on the other hand, is symptomatic of superdiffusivity and indicates that non-negligible correlations persist and advection is still relevant. In simulations of oceanic flows slopes close to -1 are commonly found at large separations in presence of shear dispersion due to the persistence of a non-zero mean relative velocity when different particles moved along separated current systems (Iudicone et al., 2002).

The FSLE curves in Fig. 14 are calculated with the fastest-crossing method (Poje et al., 2010) using the tracer positions projected on the horizontal plan. In the case of particles originated in region B it is evident a resolution dependence. In HR a slope proportional to -1 is found at large separation scales (> 60 km), while submesoscale currents contribute to the energy contained between 10 and 40 km inducing local spreading (in other words the spreading at a given separation is governed by processes at that scale) that results in slopes with $\delta \sim -2/3$ as in the case of near surface tracers (Zhong et al., 2013). In LR the curves are flatter than in HR for all separations, suggesting that at 5 km horizontal resolution spreading is driven non-locally by mesoscale eddies larger than or as large as the separation distance. For separation distances below 10 km, the HR FSLE curves flatten as well, consistent with previous modeling studies that indicate that the local processes properly captured in models are at scales 5 to 10 times the grid resolution (Zhong et al., 2013). In both integrations a perfectly flat plateau is not achieved, a known limitation of FSLE calculations performed with the fastest crossing method (Poje et al., 2010). For particles released in the De Soto Canyon, on the other hand, the FSLE slopes are generally flatter than -2/3 at both

resolutions – even if steeper in HR where a -2/3 fit may be relevant for separations comprised between 10 and 20 km -, suggesting that local submesoscale dynamics are less common along this portion of the slope at the resolution considered. Also, few pairs in A separate more than 50 km over the 100 day period of the integrations and curves become noisy for large distances. Independently of resolution, tracer spreading is significantly greater for region B than in the De Soto Canyon.

At last, we evaluated the impact of resolution on the vertical spreading of the Lagrangian tracers. Along the vertical direction to our knowledge no study has investigated FSLE, and we chose relative dispersion, R^2, to compare with results by van Aartrijk et al. (2008). R^2, defined as $R^2(t) = <|z_i - z_j|>$, where z_i nd z_j are the position of two initially nearby particles computed at the same time, and $< >$ indicates the average over all particle pairs, is shown in Fig. 15 with the corresponding diffusivities. Pairs were defined using particles in nearby grid cells and their initial vertical separation varies as function of the bathymetry. Increasing resolution corresponds to greater spreading and therefore higher relative dispersion also along the vertical direction in region B. The slopes for B curves display an intermediate regime with slope closer to $R^2 \sim t^2$ rather than to the Richardson t^3 scaling, in agreement with findings in van Aartrijk et al. (2008). In De Soto particle vertical movements are limited and strongly constrained by the bathymetry, which is identical at both resolutions, and differences between HR and LR are within the standard deviation of the sample.

The presence of boundaries and inhomogeneity limits the interpretation of the relative dispersion slope in terms of turbulence theories. Nevertheless, submesoscale currents are

known to increase energy dissipation and thus diapycnal flux, and the differences in the estimated K values at the two resolutions are at least suggestive that they might be important over slope regions.

While the vertical spreading behaviors have a plausible pattern, the diffusivity values are somewhat higher than usually measured by microstructure and dye releases. In particular they are about two times greater than measured during the deep release experiment conducted in 2012 in the vicinity of MC297 (Ledwell et al., 2016). Discrete advection errors can cause false diapycnal tracer flux in ROMS, and this might be contaminating our K estimates.

Finally, a passive dye is released in the bottom model layer near the *Deepwater Horizon* site, at MC297, and along the eastern edge of the Central Slope, at GC600 (Fig. 1). The goal of these two dye experiments is to further emphasize the complexity and variability of the circulation along the continental slope in the northern Gulf of Mexico, and to confirm the differences between the De Soto Canyon and the central and western portion of the domain, while exploring the impact of those differences on the patchiness of a passive tracer. In the following we focus on the HR case, where the tracer is released at 9 grid points with a thickness of 45 m at MC297 and 56 m at GC600.

Around the MC297 site, the near-bottom mean circulation consists of very weak cyclonic currents (less than 1 cm s^{-1}) with the lowest standard deviation in the deep domain (Fig. 10). The circulation in the immediate proximity of GC600, on the other hand, is affected by topographically constrained mesoscale eddies that form along the Mississippi slope at the site' depth and are advected towards the Central Slope (Fig. 8 and vorticity field video at 1500 m) where vorticity shows little coherency due to the complex bathymetry that quickly

erodes the submesoscale eddies.

In the case of the MC297 release (Fig. 16), three months after deployment most of the tracer can be found in the immediate proximity of the site, in a narrow 100 km long filament to the west of it and, in very small amount, in a filament the east, extending into the De Soto Canyon along the 1500 m isobaths. The tracer to the west follows the trajectory of the deep oil plume identified in June 2010 (Camilli et al., 2010). After six months most of the tracer is still within 75 km of the site, while some has spread west of the Mississippi mouth carried by the along-slope currents and by a chain of submesoscale eddies that form regularly along the 1500 m isobath to the west of the Mississippi Fan (see vorticity movies). One year after deployment the tracer occupies most of the area comprised between the 1500 and 2000 m isobaths, but it is not uniformly distributed and a significant portion (~10%) is still concentrated to the immediate south and south-west of the deployment site.

A different picture emerges at GC600. Here the intermittency in both space and time of the near bottom velocity field around the site plays an important role in the initial tracer evolution. The dye moves towards the Central slope where is quickly diffused, while continuing in its propagation mostly, but not exclusively, to the west. After one year the GC600 tracer can be found in small concentrations over most of the domain in waters deeper than 1000 m.

Figure 16, together with the similar evolution of the Lagrangian tracers in region A, suggests that the evolution of any accidental spill within the De Soto Canyon may be characterized by comparable diffusivities and overall behavior, regardless of the exact location and timing. At GC600, on the other hand, any tracer will spread much faster and the

details of its initial spreading may vary over the first month due to the highly variable zonal velocity field and to the submesoscale circulations. In light of the dispersion analysis performed and of the dye visualization, we suggest that the potential for predictability of the evolution of an accidental releases around GC600 and more broadly in the B region is limited compared to the De Soto region due to the greater variability in space and time of the advective field, and that the spreading of any spill in the central or western portion of the domain will be faster and will interest a much greater area than observed in the aftermath of the *Deepwater Horizon* event.

6. Conclusions

The occurrence and impact of submesoscale currents below 1000 m in the northern Gulf of Mexico has been investigated with two three-year-long regional simulations differing only in their horizontal resolution. In the first integration dx = 1.6 km (HR), and the submesoscale processes are partially resolved, while in the second one dx = 5 km (LR), and the submesoscale is mostly unresolved. The mean circulation is cyclonic but currents along the continental slope display complex behavior and strong variability in both speed intensity and direction. A combination of mesoscale and submesoscale eddies is generated over the continental slope. The largest eddy in both integrations is a bottom-intensified cyclone with a diameter of about 70 km. It forms by vortex stretching whenever the circulation in the anticyclonic recirculation zone over the Mississippi Slope is sufficiently strong to advect the flow over the Mississippi Fan. The submesoscale eddies that are (partially) resolved in the HR run form through instabilities of near-bottom lateral-shear layers generated by the juxtaposition of along-slope frontal currents that are highly variable in both speed and

direction, and more so for increasing resolution, or by current bottom drag on the continental slope followed by current separation and subsequent instability. Submesoscale eddies form everywhere along the continental slope and are dissipated preferentially over the Central Slope and Sigsbee Escarpment through interactions with the complex bathymetry. Those generated in the De Soto Canyon are fewer but live the longest, up to four months, being isolated from strong shear currents.

The horizontal dispersion quantified using Lagrangian tracers deployed close to the oceanic bottom is statistically indistinguishable in the two integrations as to be expected given that the space-averaged transport is driven by the almost identical (in a statistical sense) mesoscale flow. Absolute dispersion is preferentially zonal (along-slope) and greater for particles initially at the Mississippi Fan and Mississippi and Central Slopes, where the Fan cyclones can advect the tracers away from the slope into deeper waters. In the De Soto Canyon, where the 2010 *Deepwater Horizon* spill took place, the mean flow velocity and most importantly its variability are reduced compared to the rest of the domain, differences between runs at different resolution are small, and the zonal dispersion is noticeably less than in the rest of the domain. The limited transport between De Soto Canyon and the Mississippi and Central Slopes, and the greater advection and mixing that characterize the areas to the west may explain the distribution and connectivity of deep-sea mussels found at seeps along the GoM continental slope and the genetic differentiation of the species found within De Soto compared to those at all other sites (Faure et al., 2015).

Submesoscale eddies and vorticity filaments impact the representation of mixing along the slope. The partially unbalanced ($R_o > 0.5$) processes resolved only at 1.6 km resolution are responsible for local dynamics that increase relative dispersion and the steepness of the

finite-time Lyapunov exponents in the scale range between the resolved dynamics and 30-50 km. Similar conclusions on the role of submesoscale structures have been reached in mixed-layer studies (Zhong et al., 2013; Poje et al., 2014).

Overall, our results indicate that the predictability potential in the northern Gulf of Mexico in the event of another deep spill is hampered by mesoscale and submesoscale structures that form at irregular intervals along the continental slope and, outside De Soto Canyon, by the variability of the along-slope currents. While the long-term, asymptotic behavior of pollutants originating from different sites in the Gulf may be estimated (general direction of propagation, minimum and maximum times required to be advected and diffused from one location to another), the trapping in individual eddies and filaments cannot. In the aftermath of the 2010 spill those submesoscale 'patches' of hydrocarbons and dispersants were likely responsible for the spotty damage of deep coral communities (Fisher et al., 2014).

Our solutions reveal that submesoscale structures at depth are weaker than the surface ones. The difference in strength partly is due to the generally weaker mesoscale flows at depth, which are the source of submesoscale variability, and partly may be explained by the absence of an external forcing to energize the near-bottom submesoscale currents. As noted, the relative increase in intensity of the eddies and vorticity filaments with resolution and the impact of this increase on mixing are indeed comparable to what found for the mixed layer (Luo et al., 2015; Zhong et al., 2013). The increase continues at even higher resolution, as verified by preliminary runs at 500 m and 150 m (Roy Barkan, personal communication). However, in the absence of observations, we cannot validate the realism of the bottom drag parameterization that plays an important role in the formation, lifespan, and dissipation of these currents.

In conclusion, this investigation confirms that the generation of submesoscale eddies along continental slopes is a generic process, as hypothesized by Molemaker et al. (2015), likely relevant to most coastal areas, with important implications for understanding abyss-to-coast connectivity.

Appendix: Validation of near bottom model velocities

The mean circulation of the Gulf of Mexico, in both the observations and in ROMS is discussed in Cardona and Bracco (2014) for a similar configuration. A validation of the model surface currents and of the temperature and salinity distributions across the water column in the current set-up is presented in the Appendix of LBCM. Overall ROMS provides a very good representation of all mean quantities, including the Loop Current (LC) strength and evolution, the Loop Eddies detachment and propagation, the Yucatan Channel transport, mean near surface and deep currents, and the water column stratification.

The mean deep flow in the northern Gulf is not well characterized in the observations due to the paucity of data. A mean velocity reconstruction over this area has been attempted using 17 PALACE (Profiling Autonomous Lagrangian Circulation Explorer) floats deployed at approximately 900 m between 1998 and 2002 (Weatherly et al., 2004). At this depth the flow is still dominated, both in the model and in the observations, by the Loop Current. Nonetheless the velocity field derived from float trajectories supports the modeled mean cyclonic pattern, the presence of recirculation zones, and the mean speed amplitude presented in Fig. 2.

As mentioned, topographic Rossby waves with periodicities from 10 to 50 days, contribute to the variability of the deep flow of the northern Gulf (Hamilton, 2009; Kolodziejczyk et al., 2012; Pérez-Brunius et al., 2013). In the observations the variability associated to TRWs has been shown to have periodicities preferentially in the 10-20 days band for currents aligned to the 1000-1500 m isobaths, 20-30 days for currents along the 1500 - 2000 m isobaths, and around 50 days for near-bottom currents over 2300 – 2500 m (Hamilton, 2009). We verified that comparable periodicities are simulated by ROMS, despite the smoothing applied to the bathymetry, in both solutions. This is shown in Fig. A1 (HR case only), where we plot the period of the maximum of the variance-preserving spectrum for the first normalized empirical orthogonal function (EOF-1) of the zonal velocity u for each grid point at which the variance is higher than an arbitrary threshold, and over two four-months long periods at the beginning and end of the integration (similar results are obtained through other model periods). The threshold was chosen based on the observed speed spectra (Hamilton, 2009) and set to be 0.5.

Additionally, numerical simulations have shown that in the north GoM the eddy kinetic energy (EKE) to kinetic energy (KE) ratio is close to one everywhere but over the portion of the continental shelf where the water column is shallower than 200 m (Cardona and Bracco, 2014). In the northern Gulf mesoscale dynamics prevails also in the bottom layer, contributing at least 80% of the total kinetic energy.

Deep current measurements in our focus area are not abundant. They are mostly limited to the eastern end of the Central Slope, where the topography is particularly steep, with current meters deployed as early as the 1980s (Hamilton, 1990; Hamilton, 2007), and to exploratory work performed between 2003 and 2006 (Donohue et al., 2006; Hamilton, 2009). The magnitude of the modeled currents at eastern portion of the Central Slope underestimates the observations. A maximum speed of 90 cm s^{-1}, associated with the propagation of TRWs with a short period of 8-14 days, has been recorded at about 50 m from the bottom (Hamilton and Lugo-Fernandez, 2001). In contrast, modeled values attain only 50 cm s^{-1} in HR and 30 cm s^{-1} in LR, and the characteristic period over the area covering the mooring is 10-25 days. The speed underestimation is caused in part by the smoothing applied to the topographic relief to limit unphysical pressure gradient currents. We tested that values nearing 80 cm s^{-1} are achieved near the bottom along the steeper portions of the continental close in a sensitivity run performed at 1 km resolution with the bathymetry smoothed at 1 km (in this work the bathymetry is smoothed at 5 km in both runs). Longer preferred periodicities, ranging from 40 to 80 days, characterize the modeled flow south of 26.5^{o}N in the eastern portion of the domain, in agreement with previous modeling work (Oey and Lee, 2002), while 20-40 day peaks are commonly found in spectra calculated over areas covering

the slope to the west of the eastern end of Sigsbee. The periodicities are independent of resolution given that an identical smoothing is applied to the topography (not shown).

Between 2010 and 2013, the ECOGIG program collected several time series of near bottom velocities (usually 10 m from the bottom) through Acoustic Doppler Current Profilers (ADCPs) and single point current meters deployed on lander systems at the locations where the passive tracers have been released. The time series were obtained in correspondence of bathymetric features with size of few hundred meters that are not resolved by our model. Notwithstanding the modeled mean speed $\left(\sqrt{u^2+v^2}\right)$ compares reasonably well with the observed ones subsampled at the model frequency and over the same time period (MC297: ADCP =1.6 cm s^{-1}; HR = 2.8 cm s^{-1}; LR = 2.0 cm s^{-1}. GC600: ADCP 5.4 cm s^{-1}; HR = 4.1 cm s^{-1}; LR = 2.6 cm s^{-1}). Sample time-series of the meridional and zonal velocity components at the three sites on intervals overlapping with the available in-situ data are presented in Fig. A2.

Bibliography

Antonov, J.I., Seidov, D., Boyer, T.P., Locarnini, R.A., Mishonov, A.V., Garcia, H.E., Baranova, O.K., Zweng, M.M., Johnson, D.R, 2010. World Ocean Atlas 2009, Volume 2: Salinity. S. Levitus, Ed. NOAA Atlas NESDIS 69, U.S. Government Printing Office, Washington, D.C., 184 pp.

Artale, V., Boffetta, G., Celani, A., Cencini, M., Vulpiani, A., 1997. Dispersion of passive tracers in closed basins: Beyond the diffusion coefficient. Phys. Fluids, 9, 3162–3171, doi:10.1063/1.869433.

Babiano, A., Basdevant, C., Leroy, P., Sadourny, R., 1987. Single-particle dispersion, Lagrangian structure function and Lagrangian energy spectrum in two-dimensional incompressible turbulence. J. Mar. Res., 45, 107–131, doi:10.1357/002224087788400936.

Beckmann, A., Haidvogel, D., 1993. Numerical simulation of flow around a tall isolated seamount. Part I: problem formulation and model accuracy. J. Phys. Oceanogr., 23, 1736–1753.

Berloff, P. S., McWilliams, J. C., Bracco, A., 2002. Material transport in oceanic gyres. Part I : Phenomenology. J. Phys. Oceanogr., 32(3), 764–796.

Boccaletti, G., Ferrari, R., Fox-Kemper, B., 2007. Mixed layer instabilities and restratification. J. Phys. Oceanogr. 37, 2228-2250.

Bracco A., von Hardenberg, J., Provenzale, A., Weiss J., McWilliams, J.C., 2004. Dispersion and mixing in quasigeostrophic turbulence. Physical Review Letters, 92, 084501-1-4

Camilli, R., Reddy, C. M., Yoerger, D. R., Van Mooy, B. A. S., Jakuba, M. V., Kinsey, J. C., McIntyre, C. P., Sylva, S. P., Maloney, J. V., 2010. Tracking Hydrocarbon Plume Transport and Biodegradation at *Deepwater Horizon.* Science, 330, 201-206.

Capet, X., McWilliams, J.C., Molemaker, M.J., Shchepetkin, A.F. , 2008a. Mesoscale to submesoscale transition in the California current system. Part I: Flow structure, eddy flux, and observational tests, J. Phys. Oceanogr. 38, 29–43.

Capet, X., McWilliams, J.C., Molemaker, M.J., Shchepetkin, A.F., 2008b. Mesoscale to submesoscale transition in the California Current System. Part II: Frontal processes, J. Phys. Oceanogr., 38, 44–64.

Cardona Y., Bracco A., 2014. Predictability of mesoscale circulation throughout the water column in the Gulf of Mexico Deep Sea Res. II, http://dx.doi.org/10.1016/j.dsr2.2014.01.008

D'Asaro, E., Lee, C., Rainville, L., Harcourt, R., Thomas, L., 2011. Enhanced Turbulence

and Energy Dissipation at Ocean Fronts. Science 332, 318-322, doi: 10.1126/science.1201515

Debreu, L., Marchesiello, P., Penven, P., Cambon, G., 2012. Two-way nesting in split-explicit ocean models: Algorithms, implementation and validation. Ocean Modelling 49–50, 1-21.

Dee, D. P., Uppala, S. M., Simmons, A. J., Berrisford, P., Poli, P., Kobayashi, S., Andrae, U., Balmaseda, M. A., Balsamo, G., Bauer, P., Bechtold, P., Beljaars, A. C. M., van de Berg, L., Bidlot, J., Bormann, N., Delsol, C., Dragani, R., Fuentes, M., Geer, A. J., Haimberger, L., Healy, S. B., Hersbach, H., Hólm, E. V., Isaksen, L., Kållberg, P., Köhler, M., Matricardi, M., McNally, A. P., Monge-Sanz, B. M., Morcrette, J.-J., Park, B.-K., Peubey, C., de Rosnay, P., Tavolato, C., Thépaut, J.-N.,Vitart, F., 2011. The ERA-Interim reanalysis: configuration and performance of the data assimilation system. Quart. J. Roy. Meteorol. Soc. 137, 553–597.

DeHaan, C.J., Sturges, W., 2005. Deep Cyclonic Circulation in the Gulf of Mexico. J. Phys. Oceanogr. 35, 1801-1812.

Dewar, W. K., J. C. McWilliams, and M. J. Molemaker, 2015: Centrifugal instability and mixing in the California Undercurrent. J. Phys. Oceanogr., in press, doi:10.1175/JPO-D-13-0269.1.

d'Ovidio, F., Isern-Fontanet, J., López, C., Hernández-García, E., García-Ladona, E., 2009. Comparison between Eulerian diagnostics and finite-size Lyapunov exponents computed from altimetry in the Algerian Basin. Deep Sea Res., Part I, 56, 15–31, doi:10.1016/j.dsr.2008.07.014.

Drake, P. T., Edwards, C.A., Barth, J.A., 2011. Dispersion and connectivity estimates along the U.S. west coast from a realistic numerical model. J. Mar. Res., 69, 1–37, doi:10.1357/002224011798147615.

Dukhovskoy, D.S., Morey, S.L., Martin, P.J., O'Brien, J.J., Cooper, C., 2009. Application of a vanishing, quasi-sigma, vertical coordinate for simulation of high-speed, deep currents over the Sigsbee Escarpment in the Gulf of Mexico. Ocean Modelling 28, 250-265.

Elhmaïdi, D., Provenzale, A., Babiano, A. 1993. Elementary topology of two-dimensional turbulence from a Lagrangian viewpoint and single-particle dispersion. J. Fluid Mech., 257, 533–558, doi:10.1017/S0022112093003192.

Faure, B., Schaeffer, S.W., Fisher, C.R., 2015. Species distribution and population connectivity of deep-sea mussels at hydrocarbon seeps in the Gulf of Mexico. PLoS ONE 10(4): e0118460. doi:10.1371/journal.pone.0118460

Fisher, C. R., Hsing, P.-Y., Kaiser, C. L., Yoerger, D. R., Roberts, H. H., Shedd, W. W., Cordes, E. E., Shank, T. M., Berlet, S. P., Saunders, M. G., Larcom., E. A., Brooks, J. M.,

2014. Footprint of *Deepwater Horizon* blowout impact to deep-water coral communities. Proc. Nat. Acad. Sciences USA, 111, 11744–11749, doi: 10.1073/pnas.1403492111.

Fox-Kemper, B., Ferrari, R., Hallberg, R., 2008. Parameterization of Mixed Layer Eddies. Part I: Theory and Diagnosis. J. Phys. Oceanogr., 38, 1145-1165.

Garrett, C. 1983. On the initial streakiness of a dispersion tracer in two- and three-dimensional turbulence. Dyn. Atmos. Oceans, 7, 265–277.

Greene, A.D., Sutyrin, G.G., Watts, D.R., 2009. Deep cyclogenesis by synoptic eddies interacting with a seamount. J. Marine Res. 67, 305-322.

Gula, J., Molemaker, M.J., McWilliams, J.C., 2014. Submesoscale cold filamentes in the Gulf Stream. J. Phys. Oceanogr. 44, 2617-2643.

Haine, T. W. N., Marshall J. 1998. Gravitational, Symmetric, and Baroclinic Instability of the Ocean Mixed Layer. J. Phys. Oceanogr., 28, 634-658.

Hamilton, P., 1990. Deep Currents in the Gulf of Mexico. J. Phys. Oceanogr. 20, 1087-1104.

Hamilton, P., 2007. Deep-current variability near the Sigsbee Escarpment in the Gulf of Mexico. J. Phys. Oceanogr., 37, 708-726.

Hamilton, P., 2009. Topographic Rossby waves in the Gulf of Mexico. Prog. Oceanogr. 82, 1–31, http://dx.doi.org/10.1016/j.pocean.2009.04.019.

Hamilton, P., Lugo-Fernández, A., 2001. Observations of high speed deep currents in the northern Gulf of Mexico. Geoph. Res. Lett. 28, 2867-2870.

Haza, A. C., Özgökmen, T.M., Griffa, A., Z. D. Garraffo, Z.D., Piterbarg, L., 2012. Parameterization of particle transport at submesoscales in the Gulf Stream region using Lagrangian subgridscale models, Ocean Modell., 42, 31-49, doi:10.1016/j.ocemod.2011.11.005.

Hill, J., Piggott, M., Ham, D., Popova, E., Srokosz, M., 2012 On the performance of a generic length scale turbulence model within an adaptive finite element ocean model Ocean Modell., 56, 1–15.

Holmes, R. M., Thomas, L. N., Thompson, L., D. Darr D.,2014. Potential Vorticity Dynamics of Tropical Instability Vortices. J. Phys. Oceanogr., 44, 995-1011.

Huppert, H.E., Bryan, K., 1976. Topographically generated eddies. Deep-Sea Res., 23, 655–679.

Iudicone, D., Lacorata, G., Rupolo, V., Santoleri, R., Vulpiani, A., 2002. Sensitivity of numerical tracer trajectories to uncertainties in OGCM velocity fields. Ocean Modell. 4, 313–325.

Joye, S.B., MacDonald, I.R., Leifer, I., Asper, V., 2011. Magnitude and oxidation potential of hydrocarbon gases released from the BP oil well blowout. Nature Geosci. 4, 160-164.

Keating, S. R., Smith, K. S., Kramer, P.R., 2011. Diagnosing lateral mixing in the upper ocean with virtual tracers: Spatial and temporal resolution dependence. J. Phys. Oceanogr., 41, 1512–1534, doi:10.1175/2011JPO4580.1.

Klein, P., Lapeyre, G., 2009. The Oceanic Vertical Pump Induced by Mesoscale and Submesoscale Turbulence. Annual Rev. Marine Science 1, 351-375

Klocker, A., Ferrari, R., LaCasce, J. H., Merrifield, S. T., 2012. Reconciling float-based and tracer-based estimates of lateral diffusivities. J. Marine Res., 70, 569-602

Kolodziejczyk, N., Ochoa, J., Candela, J., Sheinbaum, J., 2012. Observations of intermittent deep currents and eddies in the Gulf of Mexico, J. Geophys. Res. 117, C09014, doi:10.1029/2012JC007890.

Koszalka, I., Bracco A., McWilliams, J.C., Provenzale, A., 2009. Dynamics of wind-forced coherent anticyclones in the open ocean. J. Geophys. Res. 114, C08011, doi:10.1029/2009JC005388

Large, W. G., McWilliams, J.C., Doney, S. C., 1994. Oceanic vertical mixing: a review and a model with a nonlocal boundary layer parameterization. Rev. Geophys. 32, 363-403.

Ledwell, J.R., He, R., Xue, Z., DiMarco, S.F., Spencer, L., Chapman, P., 2016. Dispersion of a tracer in the deep Gulf of Mexico. J. Geoph. Res. In Press

Ledwell, J. R., Watson, A. J., Law, C. S., 1993. Evidence for slow mixing across the pycnocline from an open-ocean tracer-release experiment. Nature, 364, 701-703.

Lee, H.-C., Mellor, G.L., 2003. Numerical simulation of the Gulf Stream System: The Loop Current and the deep circulation, J. Geophys. Res. 108(C2), 3043, doi:10.1029/2001JC001074

Lemarié, F., Debreu, L., Shchepetkin, A.F., McWilliams, J.C., 2012. On the stability and accuracy of the harmonic and biharmonic adiabatic mixing operators in ocean models, Ocean Model., 52-53, 9-35.

Lévy, M., Ferrari, R., Franks, P.J.S., Martin, A.P., Rivière, 2012. Bringing physics to life at the submesoscale. Geoph. Res. Letters 39, L14602, doi:10.1029/2012GL052756

Lévy, M., Iovino, D., Resplandy, L., Klein, P., Madec, G., Tréguier, A.-M., Masson, S., Takahashi, K., 2011. Large-scale impacts of submesoscale dynamics on phytoplankton: local and remote effects. Ocean Modelling, 44, 77–93

Lévy, M., Klein, P., Treguier, A. M., Iovino, D., Madec, G., Masson, S., Takahashi, K., 2010. Modifications of gyre circulation by submesoscale physics. Ocean Modelling 34, 1-15.

Luo, H., Bracco, A., Cardona, Y., McWilliams, J.C., 2015. The submesoscale circulation in the Northern Gulf of Mexico: Surface processes and the impact of the freshwater river input. Ocean Modelling, In Revision

MacDonald, I. R., Leifer, I., Sassen, R., Stine, P., Mitchell, R., Guinasso, N., 2002. Transfer of hydrocarbons from natural seeps to the water column and atmosphere, Geofluids 2, 95-107

Marchesiello P., Debreu, L., Couvelard, X., 2009. Spurious diapycnal mixing in terrain-following coordinate models: the problem and a solution. Ocean Modelling 26, 156-169.

McWilliams, J.C., Colas, F., Molemaker, M.J., 2009a. Cold filamentary intensification and oceanic surface convergence lines. Geophys. Res. Lett. 36, L18602, doi:10.1029/2009GL039402.

Molemaker, M. J., J. C. McWilliams, and W. K. Dewar, 2015: Submesoscale instability and generation of mesoscale anticyclones near a separation of the California Undercurrent. J. Phys. Oceanogr., 45, 613–629, doi:10.1175/JPO-D-13-0225.1.

Oey, L.-Y., Hamilton, P., 2012. Ultra-deepwater circulation processes in the Gulf of Mexico. U.S. Dept. of the Interior, Bureau of Ocean Energy Management, Gulf of Mexico OCS Region, New Orleans, LA. OCS Study BOEM 2012-004. 72 pp.

Ohlmann, J. C., Mitarai, S., 2010. Lagrangian assessment of simulated surface current dispersion in the coastal ocean. Geophys. Res. Lett., 37, L17602, doi:10.1029/2010GL044436.

Osborne, A. R., Kirwan, A. D., Provenzale, A., Bergamasco, L., 1989. Fractal drifter trajectories in the Kuroshio extension. Tellus A, 41(5), 416–435

Penven, P., Marchesiello, P., Debreu, L., Lefèvre, J , 2008. Software tools for pre- and post processing of oceanic regional simulations. Environm. Modelling & Software 23, 660-662.

Pérez-Brunius P., García-Carrillo, P., Dubranna, J., Sheinbaum, J., Candela, J., 2012. Direct observations of the upper layer circulation in the southern Gulf of Mexico. Deep-Sea Res. 85, 82-94, doi.org/10.1016/j.dsr2.2012.07.020.

Poje, A. C., Haza, A.C., Özgökmen, T.M., Magaldi, M.G, Garraffo, Z.D., 2010. Resolution dependent relative dispersion statistics in a hierarchy of ocean models, Ocean Modell., 31,

36–50, doi:10.1016/j.ocemod.2009.09.002.

Poje, A.C., Özgökmen, T.M., Lipphardt, B.L., Haus, B.K., Ryan, E.H., Haza, A.C., Jacobs, G.A., Reniers, A. J. H. M., Olascoaga, M.J., Novelli, G., Griffa, A., Beron-Vera, F.B., Chen, S.S., Coelho, E., Hogan, P.J., Kirwan, A.D. Jr, Huntley, H.S., Mariano, A.J., 2014. Submesoscale dispersion in the vicinity of the *Deepwater Horizon* spill. Proc. Natl. Acad. Sci. U.S.A. 111, 12693-12698

Provenzale, A., 1999. Transport by coherent barotropic vortices. Annu. Rev. Fluid Mech., 31, 55–93, doi:10.1146/annurev.fluid.31.1.55.

Richardson, L.F., 1926. Atmospheric diffusion shown on a distance-neighbour graph. Proc. R. Soc. London Ser. A, 110, 709–737.

Sanderson, B. G., Booth, D.A., 1991. The fractal dimension of drifter trajectories and estimates of horizontal eddy-diffusivity. Tellus A, 43(5), 334–349

Sandwell, D. T., Smith, W.H.F., 1997. Marine Gravity Anomaly from Geosat and ERS-1 Satellite Altimetry, J. Geophys. Res., 102, 10,039-10,054.

Schlag, Z. R., North, E.W., 2012. Lagrangian TRANSport model (LTRANS v.2) User's Guide. University of Maryland Center for Environmental Science, Horn Point Laboratory. Cambridge, MD. 183 pp. (available at http://northweb.hpl.umces.edu/LTRANS/LTRANS-v2/LTRANSv2_UsersGuide_6Jan12.pdf)

Shchepetkin, A., McWilliams, J.C., 2003. A method for computing horizontal pressure-gradient force in an oceanic model with a non-aligned vertical coordinate. J. Geophys. Res. 108, doi:10.1029/2001C001047.

Shcherbina, A. Y., D'Asaro, E.A., Lee, C.M., Klymak, J.M., Molemaker, M.J., McWilliams, J.C., 2013. Statistics of vertical vorticity, divergence, and strain in a developed submesoscale turbulence field, Geophys. Res. Lett. 40, 4706–4711, doi:10.1002/grl.50919.

Taylor, G. I., 1921. Diffusion by continuous movements. Proc. London Math. Soc., s2-20(1), 196–212, doi:10.1112/plms/s2–20.1.196.

Taylor, J.R., Ferrari, R., 2011. Ocean fronts trigger high latitude phytoplankton blooms. Geoph. Res. Lett., 38, L23601, doi:10.1029/2011GL049312.

Thomas, L., Ferrari, R., 2008. Friction, frontogenesis, and the stratification of the surface mixed layer, J. Phys. Oceanogr., 38, 2501-2518.

Thomas, L., Tandon, A., Mahadevan, A., 2008. Submesoscale ocean processes and dynamics, in: Eddy Resolving Ocean Modeling, edited by M. Hecht and H. Hasumi, pp. 17–38, AGU, Washington, D. C.

Thomas, L. N., Taylor, J. R. , Ferrari, R., Joyce, T. M., 2013. Symmetric instability in the Gulf Stream, Deep Sea Res. - II, 91, 96-110.

van Aartrijk, M., Clercx, H.J.H., 2010. Vertical dispersion of light inertial particles in stably stratified turbulence: The influence of the Basset force, Phys. Fluids, 22(1), 013301, doi:10.1063/1.3291678.

van Aartrijk, M., Clercx, H.J.H, Winters, K.B., 2008. Single-particle, particle-pair, and multiparticle dispersion of fluid particles in forced stably stratified turbulence, Phys. Fluids, 20(2), 025104, doi:10.1063/1.2838593.

Vukovich, F. M., 2007, Climatology of ocean features in the Gulf of Mexico using satellite remote sensing data, J. Phys. Oceanogr. 37, 689-707

Weatherly, G., 2004. Intermediate Depth Circulation in the Gulf of Mexico: PALACE float results for the Gulf of Mexico between April 1998 and March 2002. OCS Study MMS 2004-013, U.S. Dept. of the Interior, Minerals Management Service, Gulf of Mexico OCS Region, New Orleans, LA, 51 pp.

Zhong Y., Bracco, A., Villareal, T., 2012. Pattern formation at the ocean surface: Sargassum distribution and the role of the eddy field. Limn. & Ocean.: Fluid and Environ., 2, 12-27, doi:10.1215/21573689-1573372

Zhong Y., Bracco, A., 2013. Submesoscale impacts on horizontal and vertical transport in the Gulf of Mexico. J. Geoph. Res. - Oceans , 118, 5651-5668, doi:10.1002/jgrc.20402

FIGURE CAPTIONS
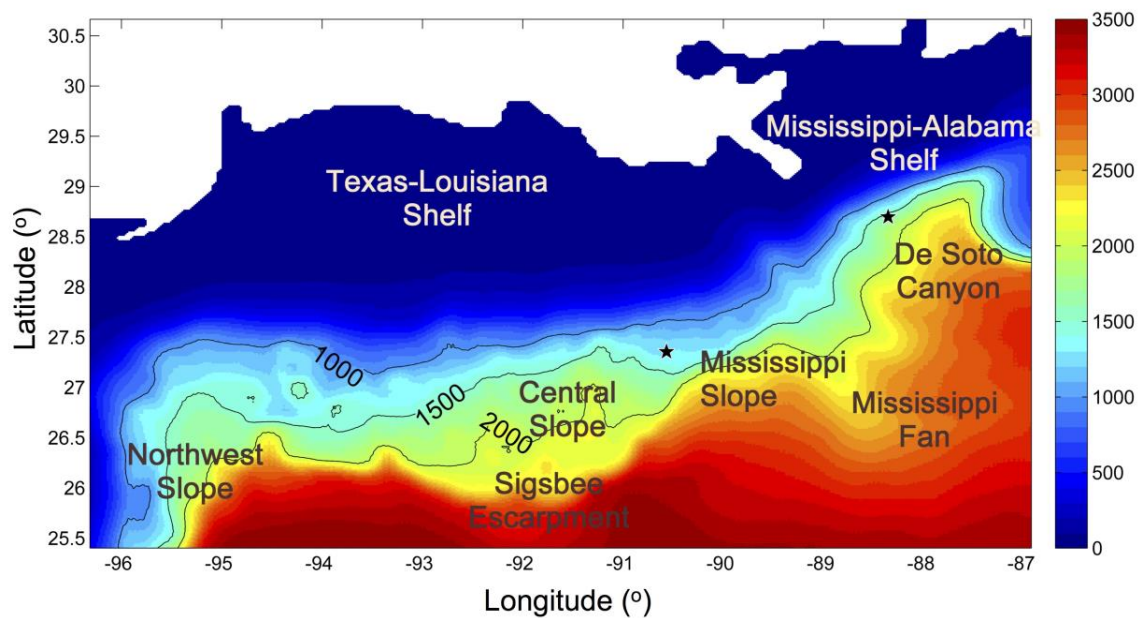
Figure 1. Bathymetry over the northern Gulf (HR) domain. The 1000, 1500, and 2000 m bathymetric contours are indicated by the black lines and major topographic features are named. The sites where the Eulerian passive tracer is released are indicated by black stars.
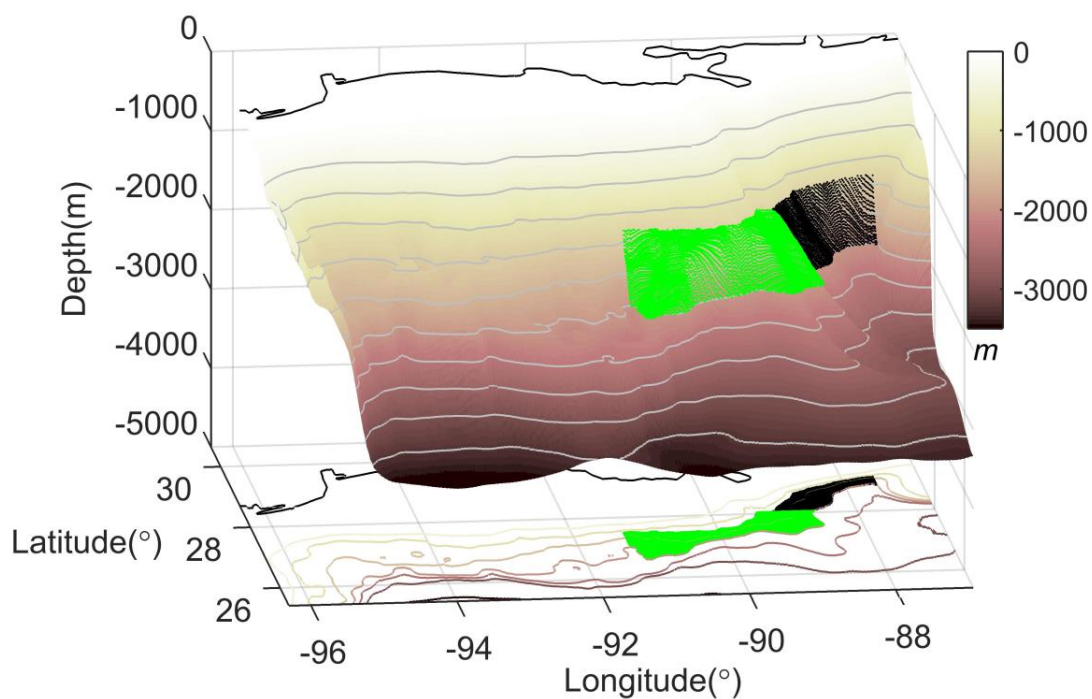
Figure 2. Initial distribution of neutrally buoyant Lagrangian particles colored according to regions A (black, De Soto Canyon) and B (green, extending from the Mississippi Fan to Green Canyon). Particles are released in the bottom model layer.
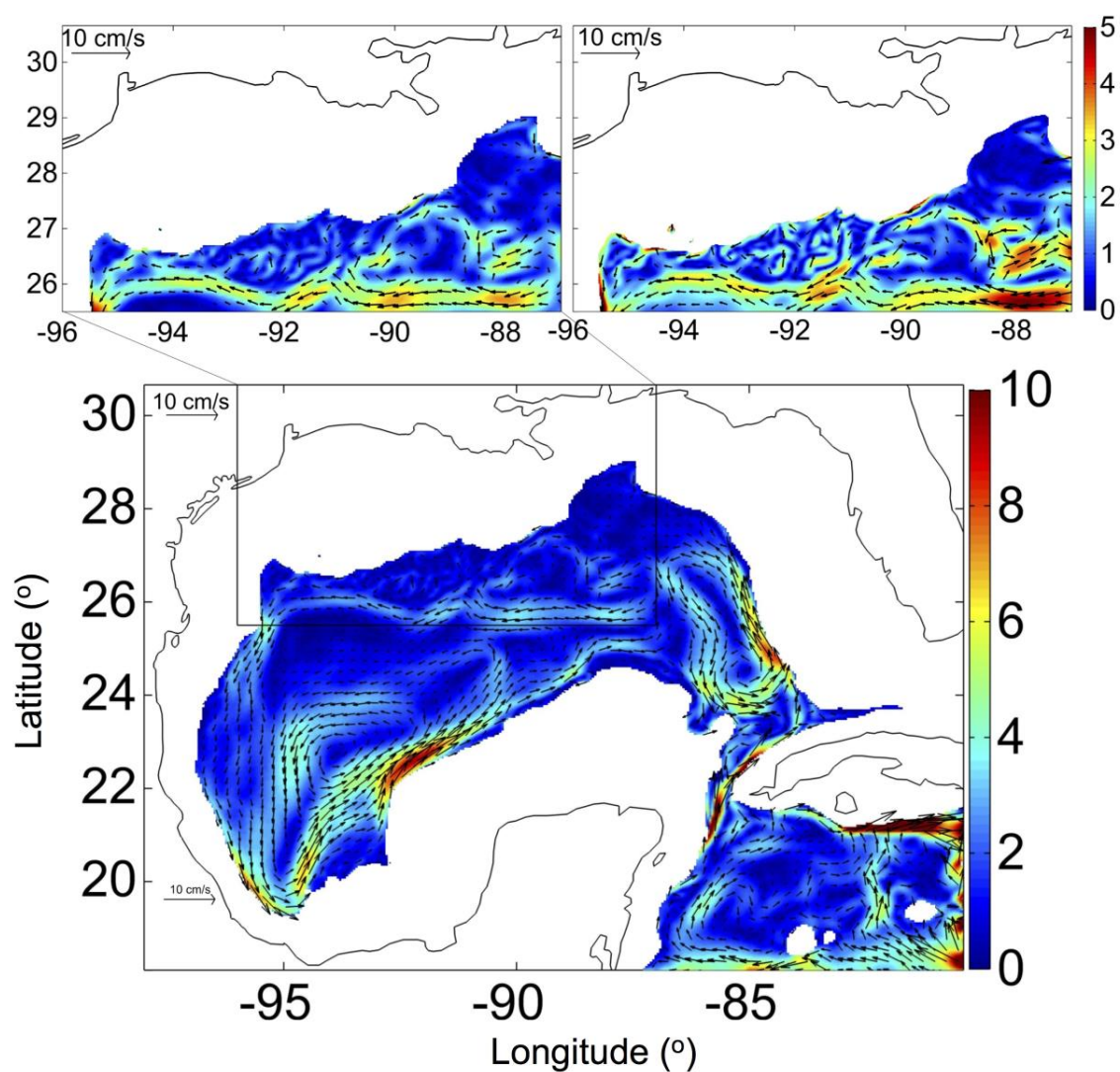
Figure 3. Mean velocity vector field in the whole Gulf of Mexico with zooms in the northern portion in both LR (top left) and HR (top right). The color bar indicates speed in cm s^{-1}.
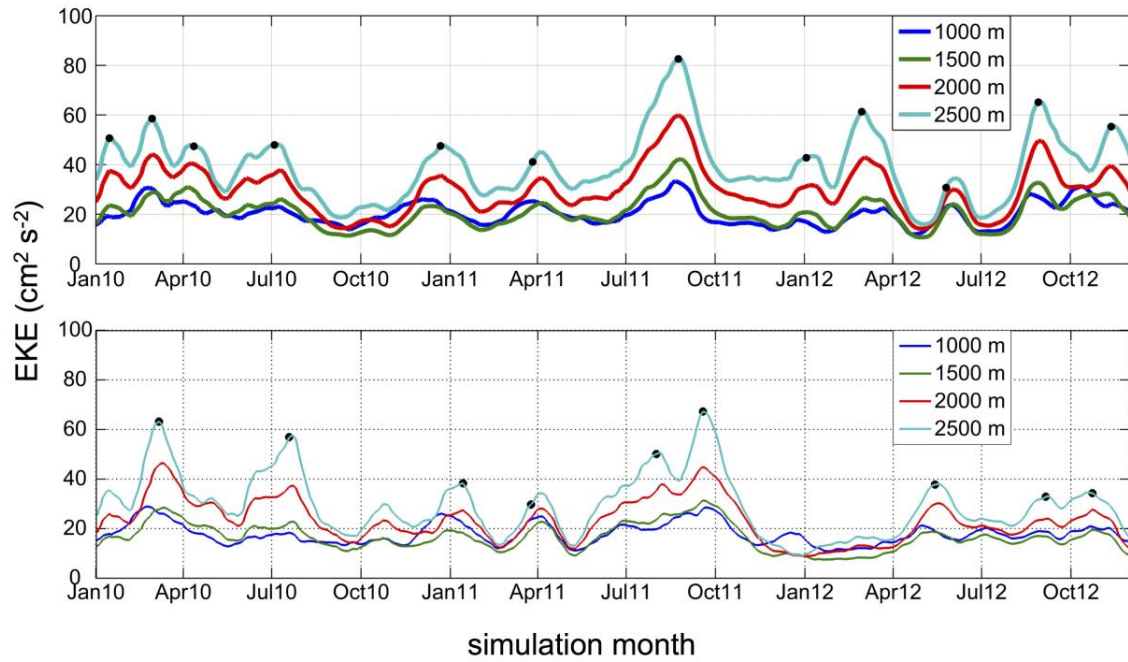
Figure 4. Eddy Kinetic Energy time series averaged over the northern Gulf at different depths across the deep layer. HR run on top (thick lines) and LR integration below (thin lines). The black dots indicate the generation of mesoscale cyclones at the Mississippi Fan.
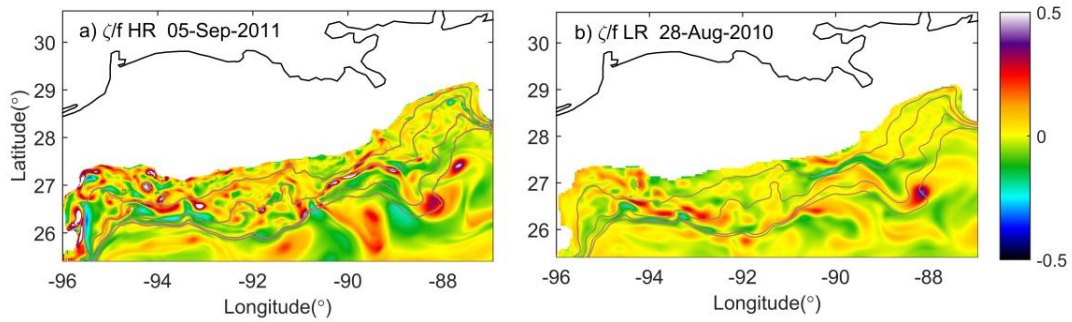
Figure 5. Snapshots of relative vorticity normalized by the Coriolis frequency, ζ/f, depth-averaged from 1000 m to the bottom. a) HR; b) LR.
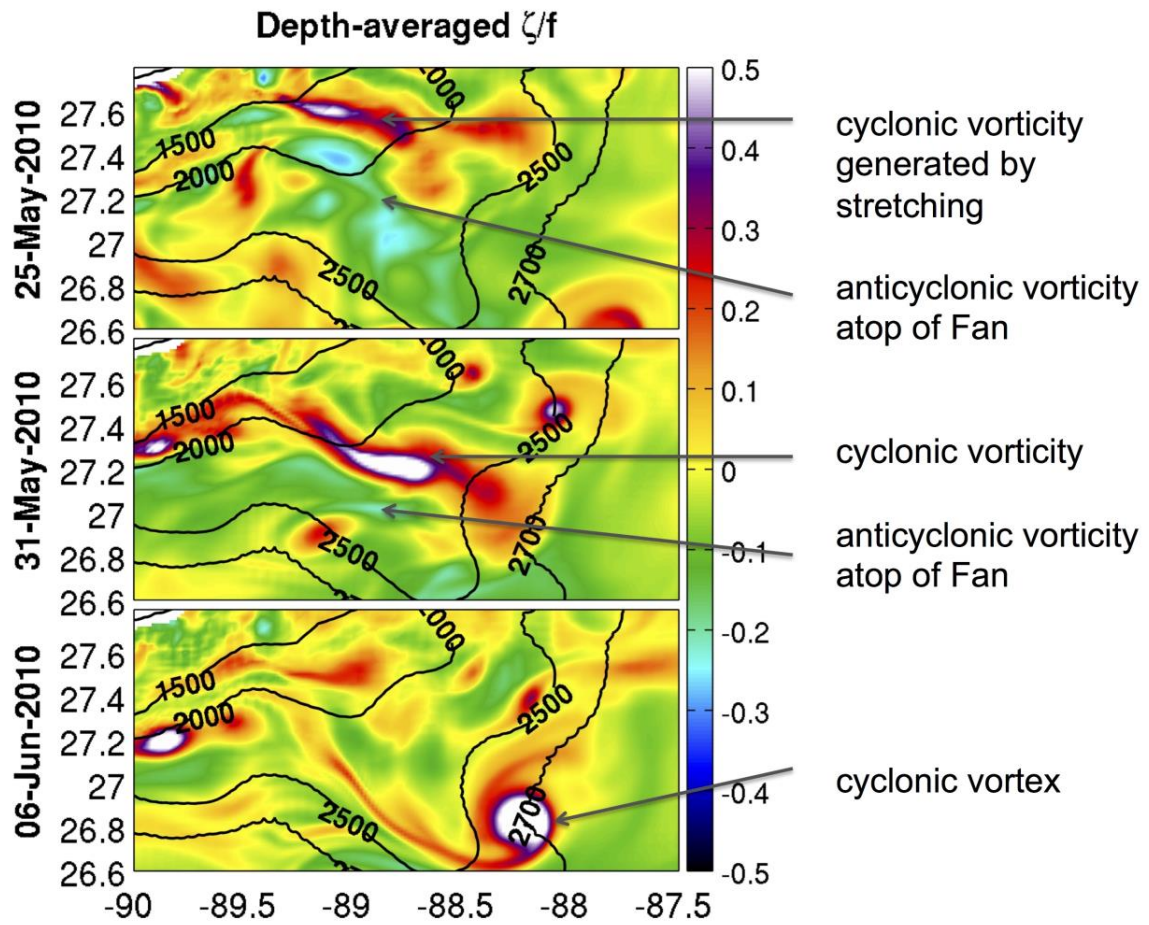
Figure 6. Snapshots of depth-averaged relative vorticity at the Mississippi Fan during the

formation of one of the mesoscale cyclones in the HR run.
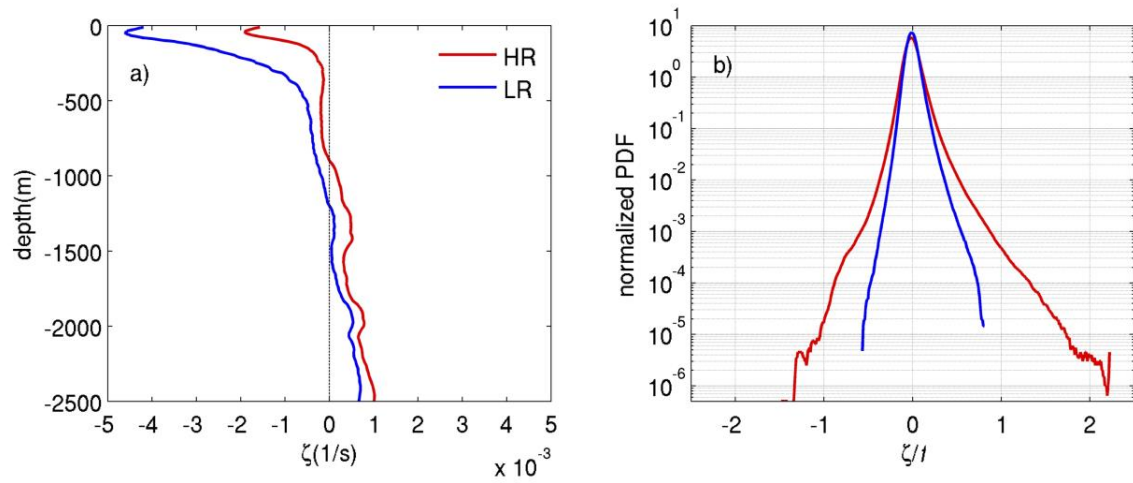
Figure 7. a) Vertical profiles of mean relative vorticity *ζ* averaged over the northern Gulf domain in HR and LR; b) PDFs of *ζ/f* in HR and LR at the depth of 1500 m, normalized to have unit integral probability. Profiles and PDFs are calculated using 360 instantaneous snapshots of vorticity (one every 3 days between January 2010 and December 2012).
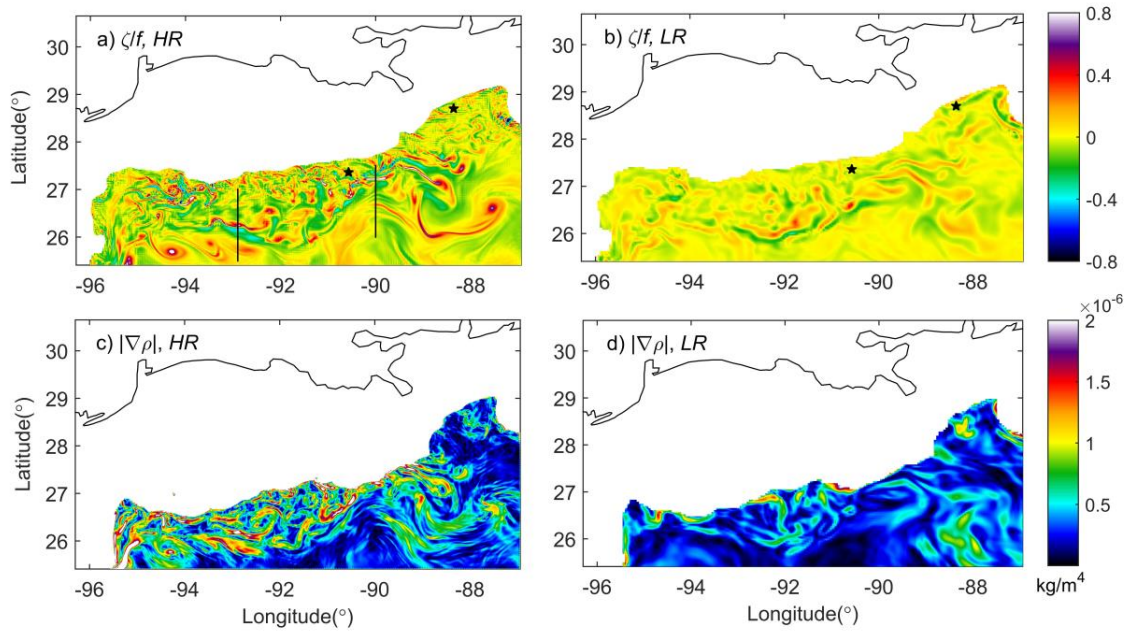
Figure 8. a)-b) Instantaneous near-bottom vorticity snapshots normalized by the Coriolis frequency on January 10, 2012 in HR and LR. c)-d) Lateral density gradients $\left|\nabla_h r\right|$ at 1500 m depth at the same time; unit km m^{-4}.
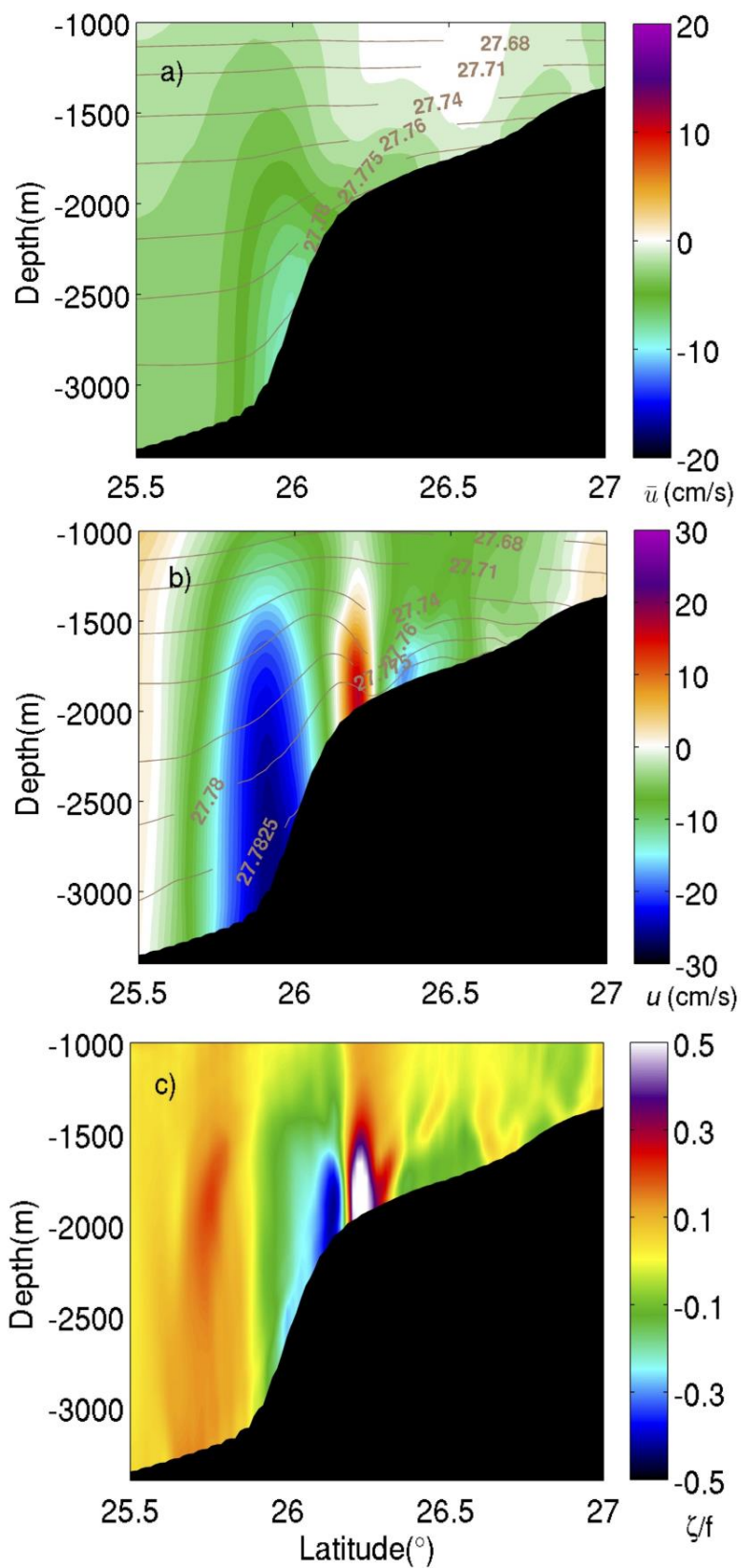
Figure 9. (a) mean (time-averaged over three years) and (b) instantaneous (on January 10, 2012) north-south transect of zonal velocity in cm s^{-1}, and (c) the corresponding instantaneous relative vorticity normalized by the Coriolis frequency along -92.9^{o}W in the HR run. Density isolines (mean or instantaneous) are superimposed on the velocity plots.
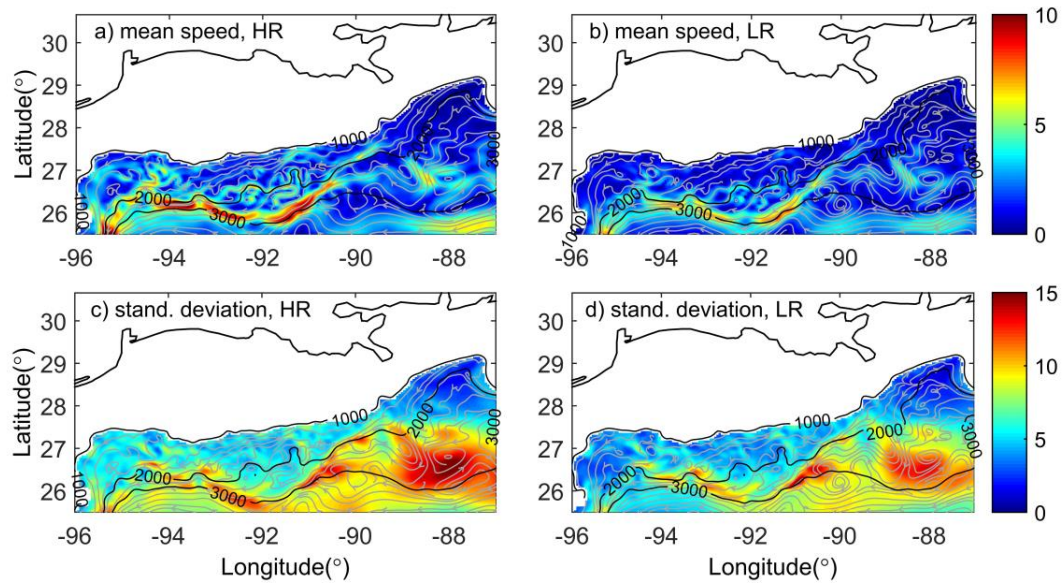
Figure 10. Near-bottom mean current speed and its standard deviation at each model grid point in HR (left) and LR (right) with superimposed horizontal velocity streamlines in the bottom model layer for depths $\geq$ 1000 m. Unit: cm s^{-1}
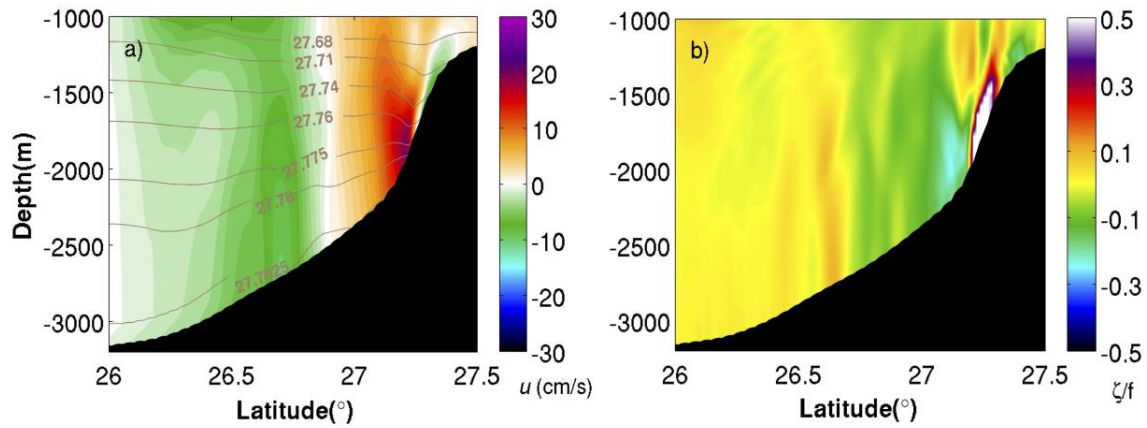
Figure 11. North-south transect on January 10, 2012 of (a) instantaneous zonal velocity in cm s^{-1}, and (b) the corresponding relative vorticity normalized by the Coriolis frequency along -90°W in the HR run. Density isolines are superimposed on the velocity plot.
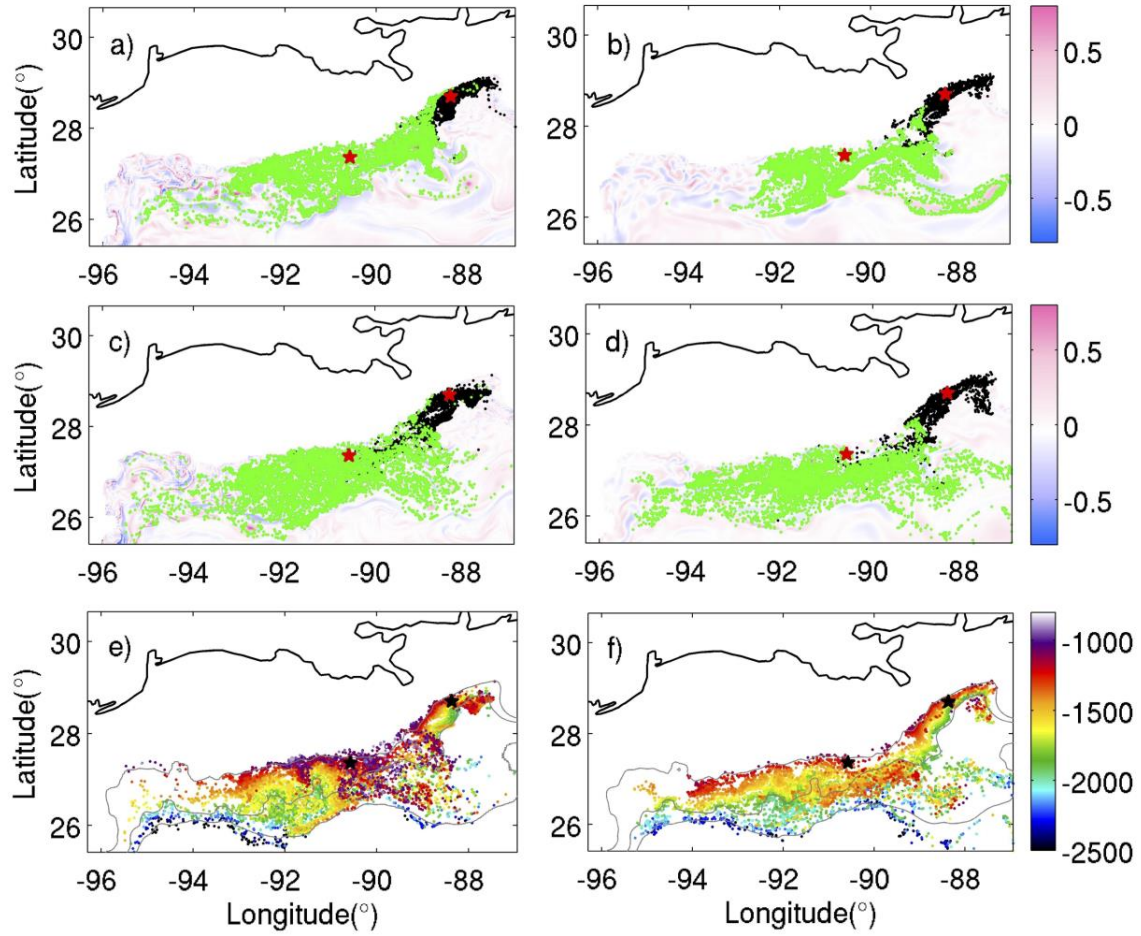
Figure 12 (a) Lateral distribution of particles superposed to relative vorticity and colored according to the deployment region (A: black, B: green) for the (a-b) April 20 and (c-d) June 10, 2010 releases. (e-f) Vertical distribution of particles colored according to their depth for the June 10, 2010 release. In both panels particles are shown 100 days after their deployment, HR on the left and LR on the right. The 1200, 2000 and 3000 m isobaths are indicated.
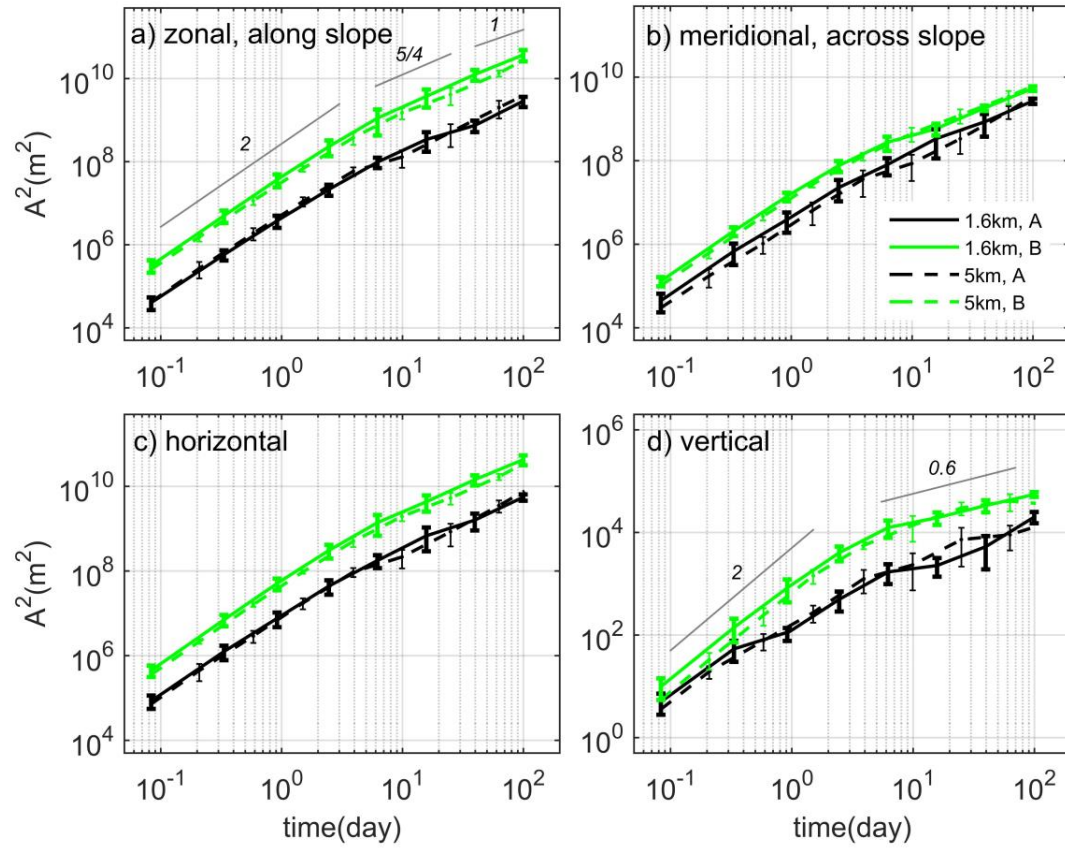
Figure 13 Along-slope, meridional, horizontal and vertical absolute dispersion of 3-D particles initially released in region A (black) and B (green) with theoretical and in the case of panel (d) best-fit slopes.
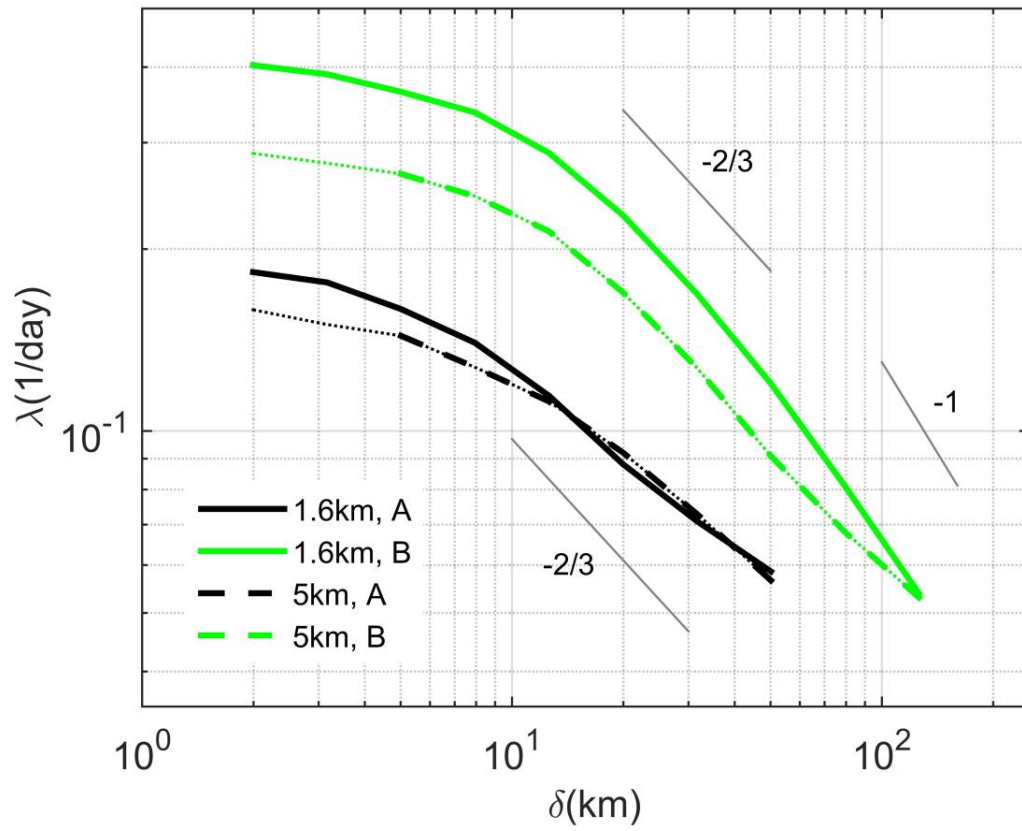
Figure 14 Finite size Lyapunov exponents of particles in region A and B at the two resolutions. Particles are deployed at a minimum distance of 1.6 km in both runs. The dotted portions of the LR curves indicate displacements below the model grid scale.
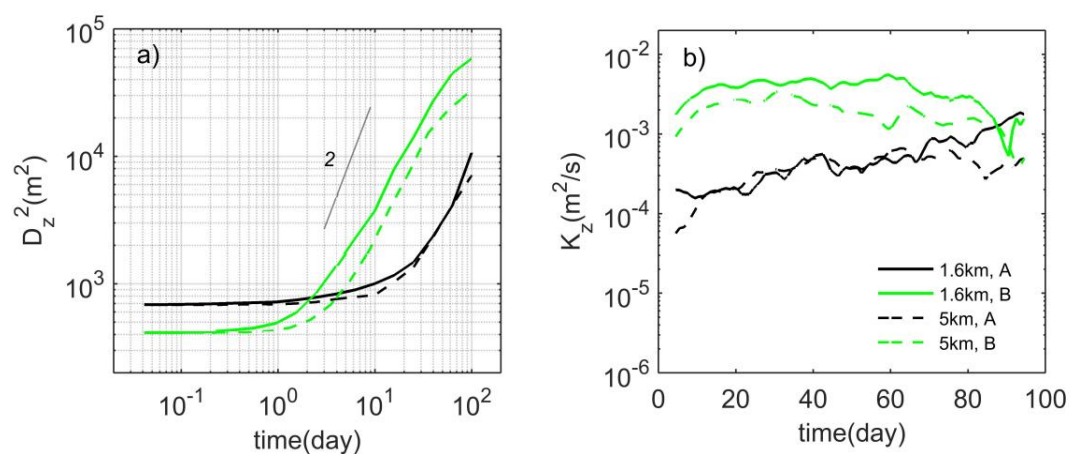
Figure 15 Vertical relative dispersion and corresponding diffusivities of 3-D particles initially released in region A (black) and B (green). The $R^2 \propto t^2$ slope is also indicated.
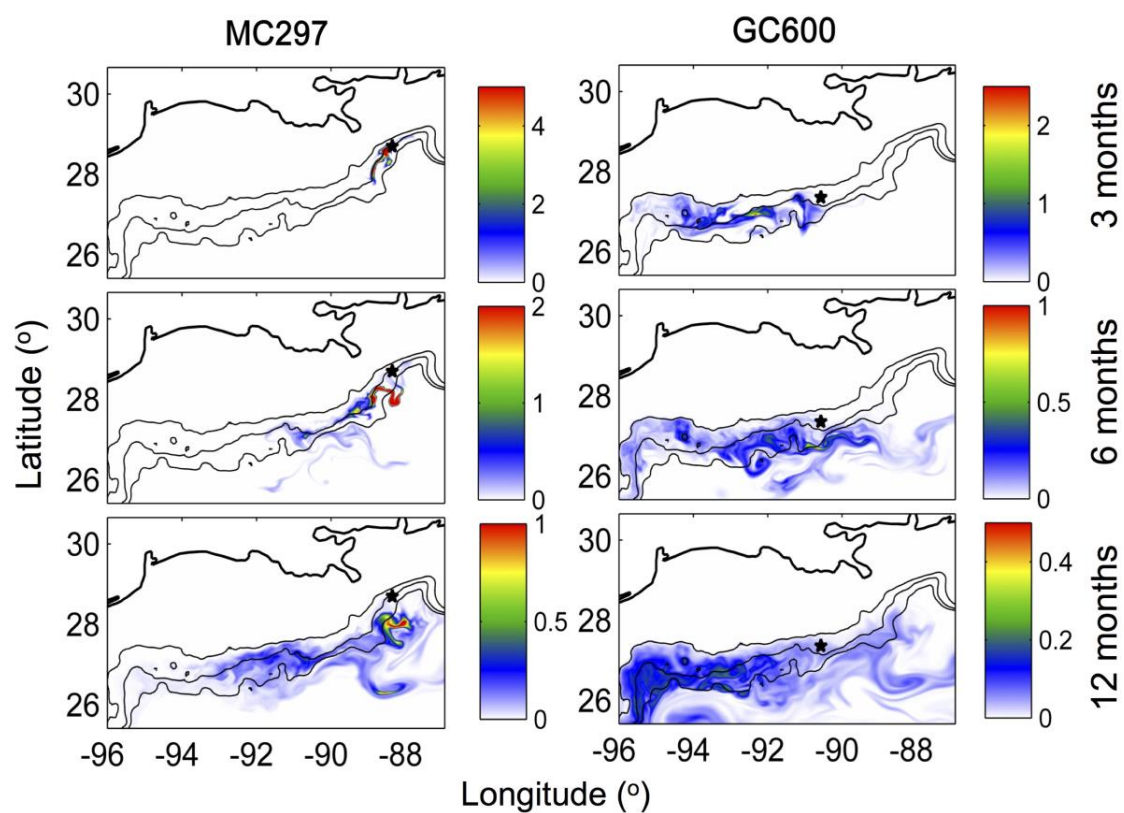
Figure 16 Depth-integrated concentration of the tracer deployed at (left) MC297 (black star) and (right) GC600 (black star) after 3, 6 and 12 months after deployment in the HR integration. The 1000, 1500 and 2000 m isobaths are also shown. Note the different color scale between left and right columns.
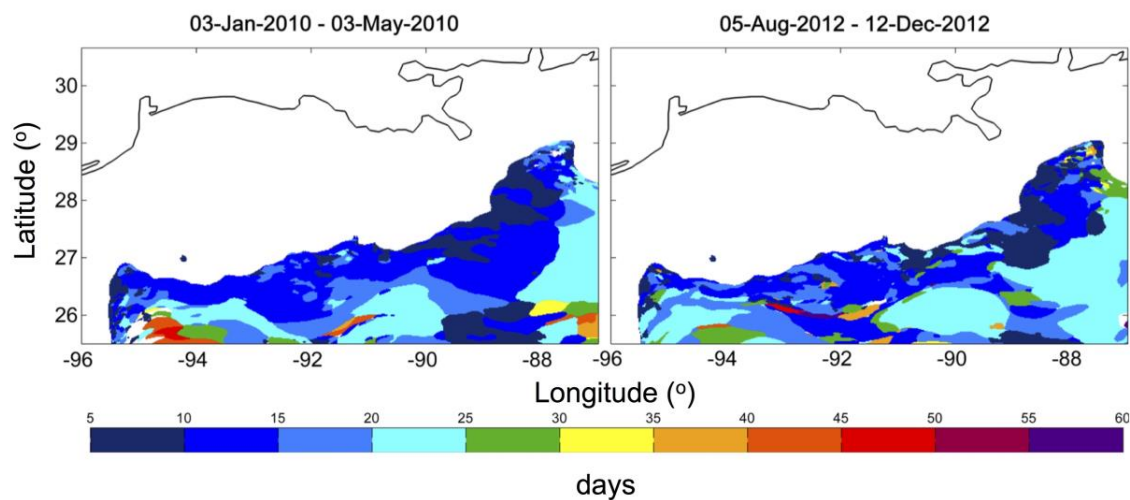
Figure A1 Maps of the period (in days) of the maximum of the variance-preserving spectrum for the normalized EOF-1 of the near-bottom zonal velocity u whenever the variance is higher than 0.5 in the HR solution. Left panel: January-May 2010; Right panel: August-December 2012.
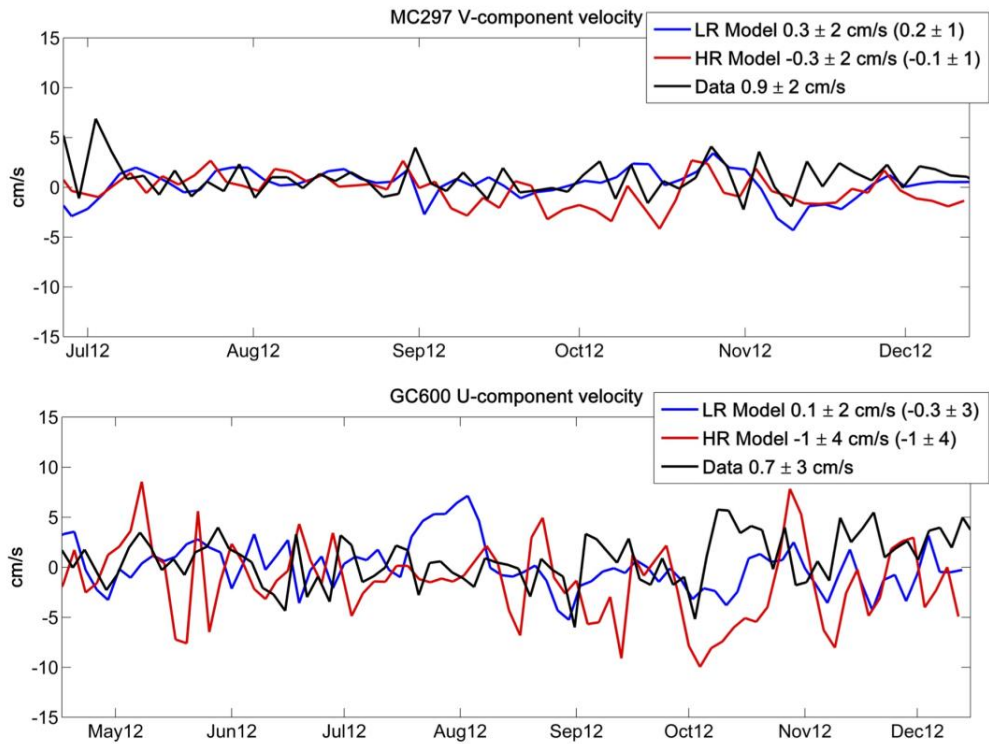
Figure A2: Sample time-series of 3-day averages of meridional (a) and zonal (b - c) velocity in cm s^{-1} in the model and in-situ data at the MC297 and GC600 sites, respectively. Mean and standard deviation calculated over the observational time frame are indicated in the legend. For the model integrations mean and standard deviation over the Jan. 2010 - Dec. 2012 period are also shown in parenthesis.